Molecular Cell

Article

YTHDC1 lactylation regulates its phase separation to enhance target mRNA stability and promote RCC progression

Graphical abstract

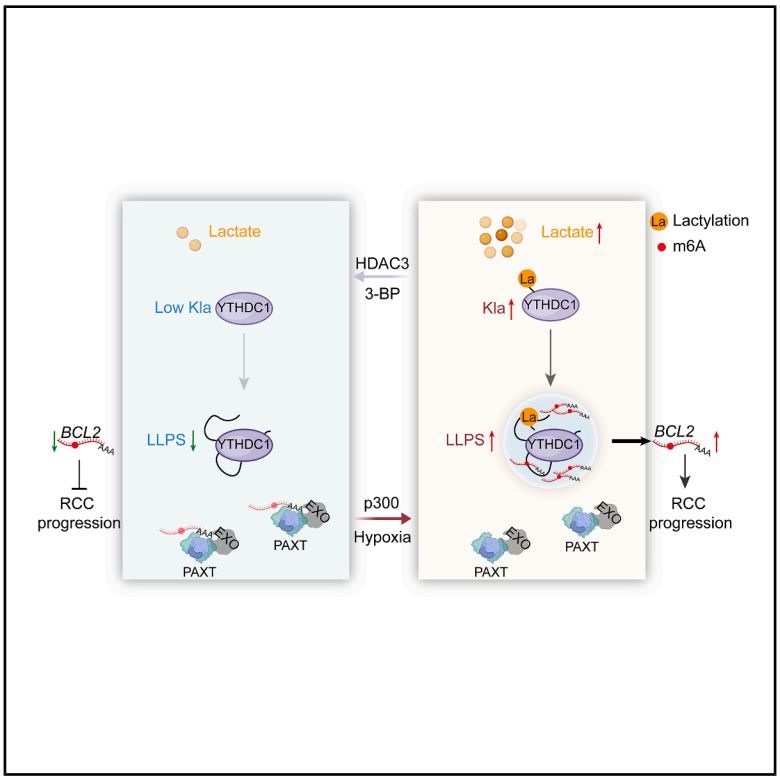

Highlights

- Quantitative lactylome analysis reveals hyperlactylated proteins under hypoxia
- Hypoxia induces p300-mediated YTHDC1 K82 lactylation to drive RCC progression
- K82-lactylated YTHDC1 enhances phase-separated condensate formation
- Condensates protect oncogenic mRNAs from degradation by the PAXT complex

Authors

Chenyun Dai (戴晨昀), Yuangui Tang (唐元桧), Huihui Yang (杨慧惠), Junfang Zheng (郑君芳)

Correspondence

zhengjf@ccmu.edu.cn

In brief

Dai et al. find that hypoxia induces protein hyperlactylation in renal cell carcinoma (RCC). p300-mediated YTHDC1 K82 lactylation promotes the expansion of phase-separated condensates. These condensates protect oncogenic BCL2 and E2F2 mRNAs from degradation by the PAXT complex to drive RCC progression.

Dai et al., 2025, Molecular Cell *85*, 2733–2748
July 17, 2025 © 2025 Elsevier Inc. All rights are reserved, including those for text and data mining, AI training, and similar technologies.
https://doi.org/10.1016/j.molcel.2025.06.017

CellPress

Molecular Cell

CellPress

Article

YTHDC1 lactylation regulates its phase separation to enhance target mRNA stability and promote RCC progression

Chenyun Dai (戴晨昀),[1,2,3,4] Yuangui Tang (唐元桧),[1,4] Huihui Yang (杨慧惠),[1] and Junfang Zheng (郑君芳)[1,5,*]

[1]Beijing Key Laboratory of Cancer Invasion and Metastasis Research, Department of Biochemistry and Molecular Biology, School of Basic Medical Sciences, Capital Medical University, Beijing 100069, China

[2]Tongji Hospital, School of Medicine, Tongji University, Shanghai 200065, China

[3]State Key Laboratory of Neurology and Oncology Drug Development, Nanjing 210018, China

[4]These authors contributed equally

[5]Lead contact

*Correspondence: zhengjf@ccmu.edu.cn

https://doi.org/10.1016/j.molcel.2025.06.017

SUMMARY

The hypoxic and lactate-enriched microenvironment of renal cell carcinoma (RCC) provides favorable conditions for aberrant lysine lactylation (Kla). However, the functional role and mechanistic basis of Kla in RCC progression remain elusive. Here, we showed an elevated global Kla level in human RCC tissues and cells, which promoted RCC malignancy. Through lactylome analysis of human RCC cells under hypoxia-mimicking conditions, we found that the m6A reader YT521-B homology (YTH) domain-containing 1 (YTHDC1) is modified by Kla at K82. YTHDC1^{K82la}, mediated by p300 under hypoxia, promotes RCC malignancy both *in vitro* and *in vivo*. Mechanistically, YTHDC1^{K82la} increases YTHDC1 phase separation, leading to the expansion of nuclear condensates and safeguarding oncogenic transcripts *BCL2* and *E2F2* from degradation by the poly A-tail exosome targeting (PAXT)-exosome complex in human RCC cells. Our results demonstrated that augmented Kla advances RCC progression by modulating phase separation and thereby regulating the stability of YTHDC1 target genes.

INTRODUCTION

Lactate, a byproduct of glycolysis, accumulates under conditions demanding rapid adenosine triphosphate (ATP) generation or hypoxia.[1] This accumulation can facilitate lactylation, a post-translational modification (PTM). Lactylation is reversibly regulated by acyltransferases (such as p300, CBP, Tip60, KAT7, KAT8, etc., with lactyl-coenzyme A [CoA] as a substrate for lactylation)[2–6] and deacylases (histone deacetylases [HDACs] and sirtuins [SIRTs]).[2,7] Recently, alanyl-tRNA synthetase 1 (AARS1) and AARS2 were reported as lactyltransferases directly utilizing lactate as a substrate for lactylation.[8,9] Lactylation of histones influences tumor progression by modulating downstream gene expression.[10–12] Moreover, non-histone proteins also undergo lactylation, regulating their functions and contributing to disease progression, including in tumors. This lactylation has been shown to regulate various biological processes such as tumor angiogenesis, homologous recombination repair, cuproptosis, endothelial-to-mesenchymal transition, and immune regulation via diverse mechanisms.[8,13–18] Given the significant role of lactylation in disease, further exploration of the impact of lactylation on cancer and its molecular basis holds significant potential.

Renal cell carcinoma (RCC), a prevalent malignant tumor of the urinary system, has been experiencing a steady rise in incidence.[19] RCC is typically unresponsive to radiotherapy and chemotherapy, and targeted therapies often lead to resistance.[20,21] Similar to other solid tumors, the hypoxic and high-lactate microenvironment in RCC provides a favorable setting for lactylation.[22] Pseudo-hypoxia phenotype observed in RCC—mutations in *VHL* and *FH* can drive a hypoxic response even in the presence of oxygen, impact histone lactylation level, and clear cell RCC (ccRCC) progression.[23] However, the specific role and mechanism of non-histone protein lactylation in RCC progression remain elusive.

YT521-B homology (YTH) domain-containing 1 (YTHDC1), a member of the YTH family, stands as the sole nucleus-localized m6A reader. It impacts alternative splicing, nuclear export, and stability of target RNAs, thereby influencing tumorigenesis.[24] Recent findings indicate that YTHDC1 undergoes biomolecular condensation.[25] This process facilitates the formation of membraneless compartments, enabling the spatiotemporal regulation of essential cellular functions such as chromatin organization, transcription, RNA processing, and translation.[26–30] These condensates can form through liquid-liquid phase separation

All rights are reserved, including those for text and data mining, AI training, and similar technologies.

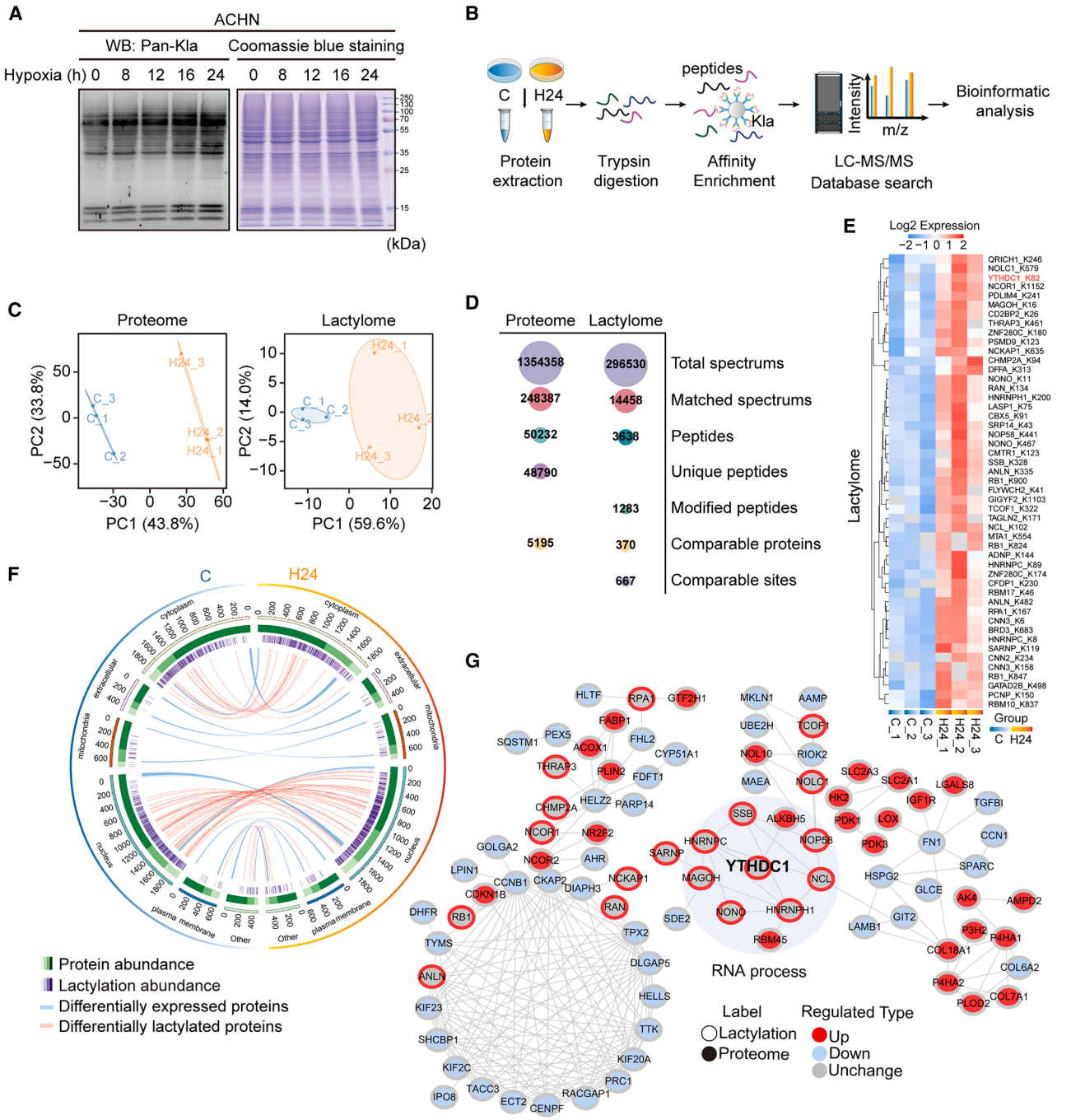

Figure 1. Comprehensive landscape of lactylation in RCC cells

(A) The Kla levels of ACHN cells treated with hypoxia for different times were detected by western blotting (WB).

(B) Schematic overview of the experimental design. Lactylated proteins in RCC cells under normoxia and hypoxia were enriched by anti-Pan-Kla antibody and identified by 4D-label-free quantitative liquid chromatography-tandem mass spectrometry (LC-MS/MS).

(C) PCA plots showing no batch effect across comparisons in the two groups (blue circle: control group; orange circle: 24 h hypoxia group). A clear separation is observed between two groups of samples.

(D) Bubble plot showing the number of Kla peptides, Kla sites, and proteins identified by 4D label-free quantitative LC-MS/MS.

(E) Heatmap of all differentially lactylated proteins in ACHN cells after 24 h hypoxia treatment (fold change > 1.5).

(F) Circos plot showing the difference in proteome and lactylome. The outermost circles represent different groups. The second circle is the subcellular localization annotation of the protein. The third circle is the abundance of proteins presented with a heatmap. The fourth circle is the abundance of Kla proteins, with

(legend continued on next page)

(LLPS), driven by weak, multivalent interactions between intrinsically disordered regions (IDRs) and nucleic acids. A wide range of physiological and pathological conditions, including tumor progression, can be impacted by condensation.[30–33]

The formation of membraneless organelles can be regulated by transcription, interactions with biomolecules such as RNA and DNA, and PTMs.[34] For instance, m6A-modified *MYC* mRNA promotes the formation of YTHDC1 nuclear condensates, safeguarding it from degradation and modulating acute myeloid leukemia (AML) progression.[25] The condensation of the YTH family is also subject to regulation by PTMs. Low O-GlcNAcylation drives the partitioning of YTHDF1/3 into stress granules, facilitating the cell's recovery from stressful conditions.[35] Recent studies have provided compelling evidence indicating that lactylation modification of DNA-binding proteins (DBPs) has the ability to attenuate LLPS. Typical examples include p53 and DNA sensor cyclic GMP-AMP synthase (cGAS).[8,9] Whether lactylation of RNA-binding proteins (RBPs) affects the phase-separated condensates remains a mystery.

This study provides a comprehensive view of hypoxia-regulated lactylation in RCC and confirms that differentially lactylated proteins induced by hypoxia in RCC are enriched in RNA processing pathways. Furthermore, we demonstrate that YTHDC1^{K82la} promotes RCC progression by modifying its condensation and selectively sequestering the transcripts of oncogenes *BCL2* and *E2F2* in condensates, thus shielding them from degradation. Targeting YTHDC1 lactylation emerges as a potential therapeutic strategy for RCC.

RESULTS

Elevated lactylation level promotes RCC malignancy

RCC cells exhibit enhanced glycolysis activity (Figure S1A), leading to the substantial production of lactate as substrates for lactylation modification (Kla). Therefore, we explored the relevance of Kla to RCC. Through immunofluorescence (IF) staining analysis of 120 pairs of renal cancer samples of different subtypes, we observed elevated pan-Kla levels in RCC tissues (Figures S1B–S1D; Table S1). Furthermore, higher global Kla level was associated with ccRCC progression and poor patient prognosis (Figures S1E and S1F; Table S1). This phenomenon was confirmed in different renal cancer cell lines compared with renal epithelial cell line (Figure S1G). These data suggest a potential association of elevated global Kla level with RCC development.

To assess the impact of lactylation on RCC development, we changed the intracellular global Kla levels of RCC cells with sodium lactate (NaLa), glycolytic inhibitor 3-bromopyruvate (3-BP, an inhibitor of hexokinase 2 [HK2]), and siLDHA/B (Figures S1H, S1I, and S1O). Importantly, fluctuations in Kla levels influenced the RCC cell malignancy (Figures S1J–S1M, S1P, and S1Q). Given that the interference in metabolic pathways may exert secondary effects on cells except for inhibiting lactate production and regulating Kla levels, we attempted to rescue the Kla level by supplementing NaLa directly in 3-BP and siLDHA/B-treated RCC cells. This treatment partially reversed the decreased RCC cell survival and proliferation by lactylation inhibitor (Figures S1N, S1P, and S1Q). To investigate the *in vivo* effects of lactylation, we administered NaLa intraperitoneally in nude mice before and after the inoculation of ACHN cells. NaLa injection led to an earlier formation of palpable tumors (about 20 mm^3) and a significant increase in tumor volume (Figures S1R–S1U). Simultaneously, the lactylation levels were markedly elevated in the NaLa injection group (Figure S1V). These findings suggest that elevated Kla levels may play a pivotal role in the malignant progression of RCC cells.

Most tumors, including RCC, thrive in a hypoxic microenvironment.[36] Under hypoxia, Kla level was increased universally in various RCC cell lines (Figure S2A). While other acylation modifications, such as acetylation, crotonylation, butyrylation, and succinylation were not elevated under hypoxia (Figures S2B–S2E). Given the importance of *VHL* mutations in RCC and their close relationship with hypoxia-inducible factors (HIFs), it is essential to investigate how *VHL* status affects hypoxia-induced lactylation in RCC. The results showed that for both *VHL*-mutated and *VHL*-unmutated cells, lactylation levels were elevated under hypoxia and in an O_2 concentration-dependent manner, even for *HIF1*-deficient 769-P cells (Figure S2F). Notably, after the ablation of HIFs, the hypoxia-induced lactylation level was not reversed to that in normoxia (Figure S2G), proving the existence of a HIF-independent pathway under hypoxia for increasing Kla levels.

Comprehensive landscape of lactylation in RCC cells

To explore the key Kla proteins that promoted RCC progression, we used hypoxia treatment to induce the lactylation microenvironment for cells. Interestingly, multiple protein bands spanning a wide mass range were detected in RCC cells, indicating the lactylation in multiple types of non-histone proteins. Like in histones, the Kla levels in non-histone proteins were gradually upregulated with the elongation of hypoxia treatment time (Figure 1A). To obtain the global landscape of lactylation in hypoxia-treated RCC cells, we treated cells with 24 h hypoxia to induce the maximum amount of hyperlactylated proteins and performed proteome and lactylome detection (Figure 1B).

The results demonstrated excellent reproducibility in both proteome and lactylome datasets, as indicated by the Pearson correlation coefficient (PCC) and the relative standard deviation (RSD) (Figures S3A and S3B), ensuring data validity. Principal-component analysis (PCA) of the proteome and lactylome data showed that the control normoxia samples (C group) and the hypoxia 24 h samples (H24 group) formed a cluster, respectively, and two clusters were clearly separated (Figure 1C). Sample quality control (QC) was rigorously conducted, including assessments of peptide length distribution, molecular

each vertical line (purple) representing 1 protein. The depth of color indicates the number of corresponding modification sites. The innermost lines represent the DEPs and Kla proteins.
(G) PPI network showing the proteins clustered in the RNA processing pathway.
See also Figures S1–S3 and Tables S1 and S2.

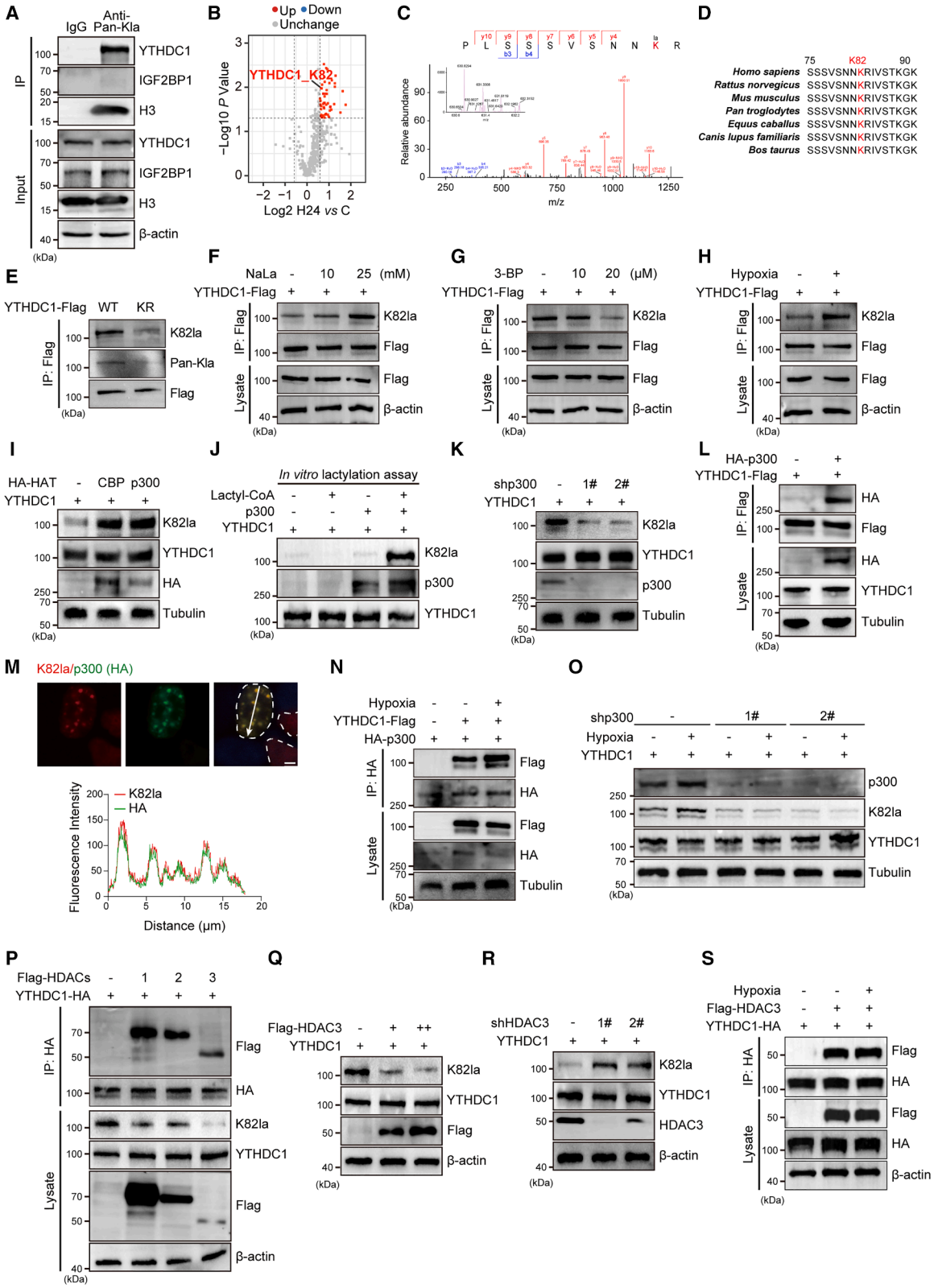

(legend on next page)

weight distribution, and the number of peptides (Figures S3C–S3E).

The proteome analysis successfully quantified 5,195 proteins. The lactylome analysis quantified 370 proteins and 667 lactylation sites (Figure 1D). The analysis of differentially expressed proteins (DEPs) in the H24 vs. C samples identified 74 upregulated and 133 downregulated proteins (Figure S3F). DEPs are widely distributed in various organelles (Figure S3G). Gene Ontology (GO) enrichment analysis provided insights into the potential functions of DEPs (Figure S3H).

Lactylation levels of 49 sites in 42 proteins were upregulated in the H24 vs. C group (Figure 1E; Table S2), and no proteins or sites were downregulated in Kla levels. Approximately 70% and 24% of differentially lactylated proteins were localized in the nucleus and cytoplasm, respectively (Figure S3I). This indicates that lactylation induced by hypoxia predominantly modifies proteins in the nucleus. A circos plot illustrated a comprehensive landscape of the proteome and lactylome analyses (Figure 1F). Interestingly, the differentially lactylated proteins showed no overlap with DEPs, indicating that hypoxia-induced lactylation may not affect the expression levels of proteins. The protein-protein interaction (PPI) network analysis of both the proteome and lactylome datasets showed that the differentially lactylated proteins were primarily associated with nucleic acid and RNA processing pathways (Figure 1G). Analysis results of the Clusters of Orthologous Groups (COGs) classification and GO showed that differentially lactylated proteins were enriched in various biological processes such as RNA processing and modification (Figures S3J and S3K). These results suggest a potential interaction between lactylation and RNA-related cellular functions.

YTHDC1^{K82} is prominently lactylated under hypoxia

Lactylated YTHDC1 immediately triggered our interest, as YTHDC1 can bind with target mRNA to regulate their alternative splicing, nuclear export, stability, and decay, thereby influencing the progression of cancer.[37–39] Its lactylation was validated by anti-pan-Kla antibody immunoprecipitation followed by anti-YTHDC1 antibody detection. The results demonstrated that endogenous YTHDC1, but not control protein IGF2BP1 (for which lactylation was not detected in multiple lactylome),[5,8,40] could be lactylated (Figures 2A and S4A). Lysine 82 (K82) was the only lactylation site in YTHDC1, which had a mass shift of 72.021 Da and is highly conserved across species (Figures 2B–2D). Meanwhile, we conducted a quantification analysis based on the parallel reaction monitoring (PRM) and found that the lactylation percentage of K82 accounted for about 0.60% of total YTHDC1 (Figure S4B).

To investigate the change of YTHDC1^{K82la} level, a rabbit polyclonal antibody specifically targeting lactylated lysine 82 (K82la) of YTHDC1 was generated using the synthetic peptide C-VSNNK$_{la}$RIVS. The dot blot analysis showed that E17780 had a good recognition ability for the lactylated peptide but not for the acetylated peptide and control peptide (Figures S4C and S4D). In addition, mutation of K82 to R82 (lysine to arginine, mimicking the de-lactylation state) resulted in a greatly decreased K82 lactylation level (Figure 2E), indicating that the anti-K82la antibody has a good specificity for recognizing K82 lactylation. Furthermore, YTHDC1^{K82la} level was increased under NaLa treatment and decreased under 3-BP treatment in a dose-dependent manner (Figures 2F and 2G), confirming that YTHDC1^{K82} can be lactylated. After 24 h of hypoxic treatment, the lactylation level of YTHDC1-wild type (WT), but not the mutant, was increased and exhibited an O_2 concentration-dependent manner (Figures 2H, S4E, and S4F). This suggests YTHDC1^{K82la} level is dynamically regulated.

p300 and HDAC3 are the regulators for the lactylation level of YTHDC1^{K82}

Histone lactylation is regulated by the acyltransferase p300 and deacylases HDACs.[7] Whether YTHDC1 lactylation is regulated

Figure 2. YTHDC1^{K82} is prominently lactylated under hypoxia, and its level is upregulated by enhanced interaction with p300

(A) Identification of lactylation in endogenous YTHDC1. Lysates of ACHN cells were immunoprecipitated with anti-Pan-Kla antibody or control IgG. WB analysis was performed with anti-YTHDC1, anti-IGF2BP1, anti-H3, and anti-β-actin in order. H3: positive control; IGF2BP1: negative control.

(B) Volcano plot showing the lactylome changes of ACHN cells in hypoxia vs. normoxia. The vertical and horizontal dashed lines denote the cutoff values (−0.58 and 0.58) for $\log_2$ (hypoxia 24 h/control ratio) and p value (<0.05), respectively.

(C) MS/MS spectra of the lactylated YTHDC1 peptide for the identification and quantification of K82 lactylation on YTHDC1. b and y ions indicate peptide backbone fragment ions containing the N and C termini, respectively. Lactylated lysine is colored in red.

(D) Alignment of protein sequences surrounding K82 in YTHDC1 across different species.

(E) ACHN cells were transiently transfected with the YTHDC1^{WT} or YTHDC1^{KR} plasmid and were then subjected to coimmunoprecipitation (coIP) with the indicated antibodies.

(F–H) ACHN cells were transiently transfected with the YTHDC1^{WT} plasmid and treated with the corresponding conditions, and then the YTHDC1^{K82la} level was measured by WB.

(I) Screening for the "writer(s)" of YTHDC1 lactylation by transfecting both YTHDC1 and acyltransferase as indicated.

(J) Detecting YTHDC1^{K82la} using an *in vitro* lactylation assay on the indicated samples.

(K) Lysates from shControl or p300 knockdown cells were tested for YTHDC1^{K82la}.

(L and M) The interaction between YTHDC1 and p300 as indicated by coIP (L) and IF (M).

(N) HA-p300 and YTHDC1-FLAG were transfected as indicated, and cells were treated with 24 h hypoxia, and the interaction of p300 with YTHDC1 was examined.

(O) shControl or p300 knockdown cells were cultured in 1% oxygen for 24 h, and lysates were immunoblotted.

(P) HEK293T cells were transfected with plasmids as indicated, immunoprecipitation was used to detect the interaction of HDAC1–3 with YTHDC1, and YTHDC1^{K82la} level in lysate.

(Q and R) YTHDC1^{K82la} level was detected with different amounts of HDAC3 (Q) and HDAC3 knockdown (R).

(S) The interaction between HDAC3 and YTHDC1 was assessed by coIP under normoxia or 24 h hypoxia.

See also Figure S4.

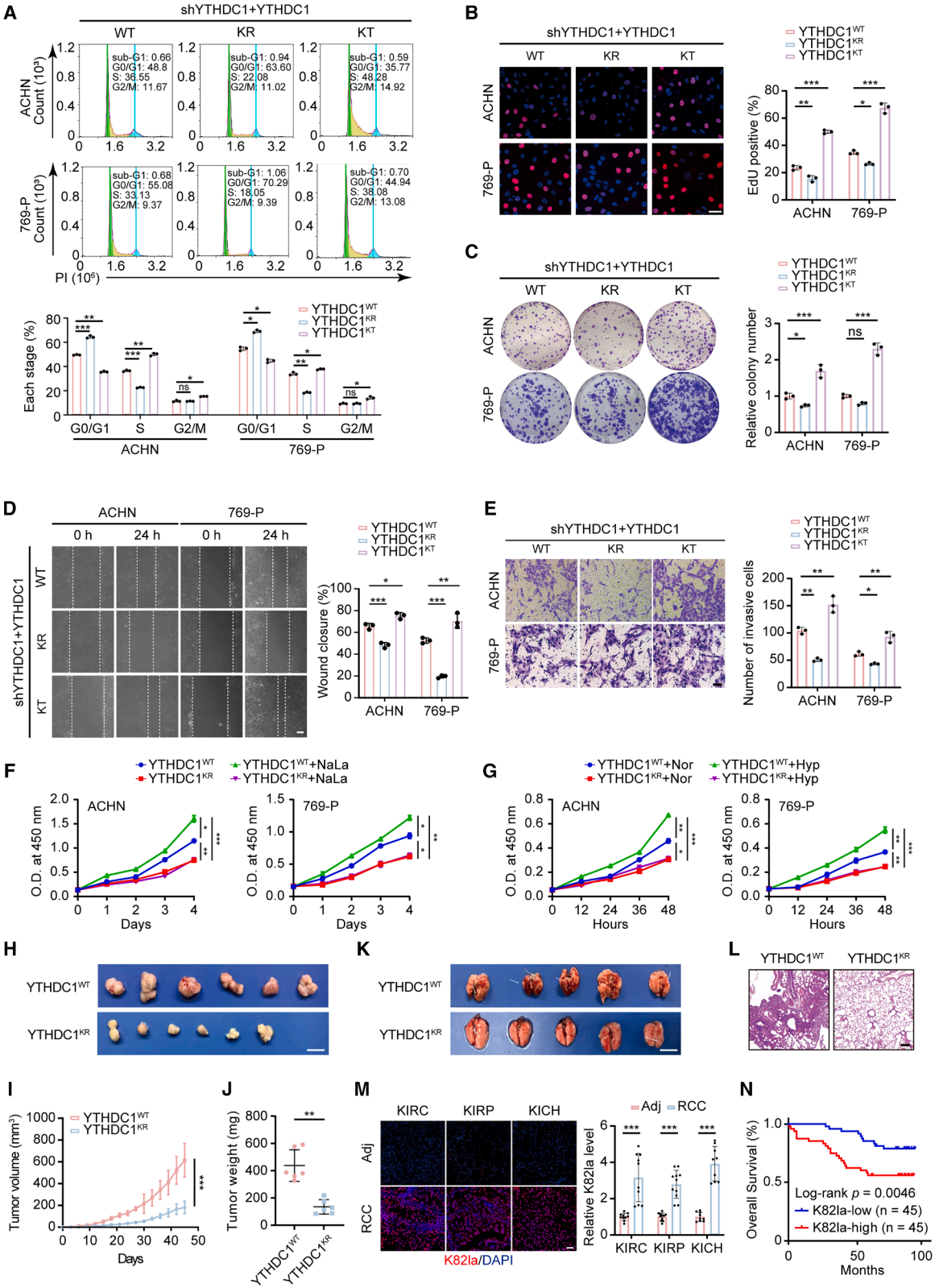

(legend on next page)

by these enzymes remains unknown. Our results showed that both p300 and CBP enhanced YTHDC1^{K82la} level (Figure 2I), and other acyltransferases such as KAT8, KAT2B, and KAT5 did not regulate the YTHDC1^{K82la} level (Figure S4G). Furthermore, p300-mediated upregulation in YTHDC1^{K82la} level was confirmed with an *in vitro* lactylation assay (Figures 2J and S4H). Conversely, the depletion of p300 resulted in a substantial reduction in YTHDC1^{K82la} level (Figure 2K). Exogenous co-immunoprecipitation unveiled the interaction between p300 and YTHDC1, and IF showed the colocalization of p300 with YTHDC1^{K82la} (Figures 2L and 2M). Additionally, hypoxia treatment enhanced the interaction between YTHDC1 and p300, and the depletion of p300 abolished the augmentation of YTHDC1^{K82la} level under hypoxia (Figures 2N and 2O). These findings suggest that p300 possesses the capability to perceive cellular hypoxia and lactylate YTHDC1^{K82}, a process crucial for the hypoxia response.

To elucidate the delactylase of YTHDC1, we treated HEK293T cells with HDAC inhibitor trichostatin A (TSA) or sirtuins inhibitor nicotinamide (NAM). YTHDC1^{K82la} level exhibited an increase under TSA treatment (Figure S4I), suggesting that YTHDC1 can undergo delactylation and the delactylases for YTHDC1 are HDACs. To identify which HDAC delactylates YTHDC1^{K82}, we co-transfected YTHDC1 with HDACs. HDAC1–3, but not HDAC4–9, overexpression had a delactylation effect on YTHDC1^{K82}, and the effect of delactylation was the most obvious for HDAC3 (Figures 2P and S4J). Simultaneously, HDAC1–3 co-immunoprecipitated with YTHDC1 (Figures 2P and S4K), suggesting the delactylation is dependent on the interaction. HDAC3 overexpression delactylated YTHDC1^{K82} in a dose-dependent manner (Figure 2Q). Knockdown of HDAC3 increased YTHDC1^{K82la} level (Figure 2R). Unlike p300, hypoxic treatment did not affect the interaction between HDAC3 and YTHDC1 (Figure 2S). These data indicate that YTHDC1^{K82la} level is reversibly regulated by p300 and HDAC3, and hypoxia promotes the elevation of YTHDC1^{K82la} level via enhancing the interaction of p300 with YTHDC1.

YTHDC1^{K82} lactylation promotes RCC malignancy

Since the lactylation occurs at K residue, we mutated K82 to arginine (YTHDC1^{KR}) or threonine (YTHDC1^{KT}), which mimicked the delactylated or hyperlactylated state of protein, and established RCC cell lines stably expressing YTHDC1$^{WT/KR/KT}$ in YTHDC1 knockdown RCC cells (Figures S5A and S5B). YTHDC1^{KT}-rescued cells exhibited more S-phase entry and an increase in cell malignancy compared with YTHDC1^{WT}-rescued cells. By contrast, the YTHDC1^{KR}-rescued group exhibited more G0/G1-phase arrest and inhibitory effects on RCC cell malignancy (Figures 3A–3E). Additional NaLa and hypoxia treatment modulated the proliferation of YTHDC1^{WT}-rescued cells but not YTHDC1^{KR}-rescued cells (Figures 3F and 3G).

Xenograft assay was conducted to assess the impact of YTHDC1^{K82la} on RCC malignancy *in vivo*. All nude mice were regularly injected intraperitoneally with NaLa to establish an *in vivo* high-lactate environment and elevate the Kla level of intratumoral YTHDC1^{WT} (Figure S5C). Compared with the ACHN-shYTHDC1-YTHDC1^{KR} group, ACHN-shYTHDC1-YTHDC1^{WT} promoted tumor growth up to 243% and 177% in volume and weight, respectively (Figures 3H–3J). In addition, Ki67 staining indicated that the proliferation ability of the WT group was stronger than the KR group (Figure S5D). Concurrently, tail-vein lung metastasis mice models injected with ACHN-shYTHDC1-YTHDC1^{WT} exhibited cachexia and more emaciation. Exploratory laparotomy revealed more lung metastasis in ACHN-shYTHDC1-YTHDC1^{WT}-injected mice (4/5) compared with ACHN-shYTHDC1-YTHDC1^{KR}-injected mice (1/5) (Figures 3K and 3L). Due to the concealed nature of many metastatic shadows in the WT group within the lung tissue or interconnected metastatic cells, statistical analysis on the number of metastases was not performed. These results affirm the crucial role of YTHDC1^{K82la} in contributing to RCC growth and metastasis. In addition, YTHDC1^{K82la} level was elevated in RCC tissues and correlated with poor prognosis of ccRCC patients (Figures 3M and 3N), suggesting that YTHDC1^{K82la} promotes RCC malignancy at the clinical level.

Meanwhile, YTHDC1^{KT}-rescued cells showed poor response to the targeted drug sunitinib (Figure S5E). Treatment with additional NaLa, hypoxia, and p300 inhibitors did not alter drug sensitivity in YTHDC1 mutants (Figures S5F–S5H). For xenografts with intraperitoneal injection of NaLa and highly lactylated YTHDC1, the combined treatment of sunitinib and 3-BP resulted in superior efficacy in slowing down tumor growth and decreasing tumor sizes and weight compared with the mono-treatment groups (Figures S5I–S5L).

Lactylation enlarges YTHDC1 nuclear condensates

To investigate the mechanism by which YTHDC1^{K82la} regulated RCC malignancy, we analyzed its structure. YTHDC1 features

Figure 3. YTHDC1^{K82la} promotes RCC malignancy

(A–E) YTHDC1^{K82} mutants regulated RCC cell cycle (A, flow cytometry PI staining), cell proliferation (B, 5-Ethynyl-2'-deoxyuridine [EdU] staining), colony formation (C, plate colony formation assay), migration (D, wound healing assay), and invasion (E, transwell invasion assay). Scale bars, 50 μm.

(F and G) Cell proliferations of YTHDC1^{WT} or YTHDC1^{KT} cells cultured with/out NaLa (F) and normoxia/hypoxia treatment (G) were measured with Cell Counting Kit-8 (CCK-8) assay.

(H–J) ACHN-shYTHDC1-YTHDC1^{WT} and ACHN-shYTHDC1-YTHDC1^{KR} were subcutaneously injected into nude mice for xenograft tumor experiments, and NaLa was injected intraperitoneally at regular intervals. Tumor images (H), tumor growth curves (I), and tumor weights (J) were shown. Scale bar, 1 cm.

(K and L) *In vivo* lung metastasis of ACHN-shYTHDC1-YTHDC1^{WT} and ACHN-shYTHDC1-YTHDC1^{KR} cells. Lung images (K) and H&E staining (L). Scale bars, 1 cm (K) and 200 μm (L).

(M) Representative IF staining results and statistical results for K82la in paired RCC samples were shown in the left and right panels, respectively. Scale bars, 50 μm.

(N) Kaplan–Meier plot for K82la level in RCC.

Analyses were performed using one-way ANOVA (A–E), two-way ANOVA (F, G, and I), unpaired two-tailed Student's t test (J), and paired two-tailed Student's t test (M). $^{*}p < 0.05$, $^{**}p < 0.01$, $^{***}p < 0.001$, ns: not significant. Data are shown as mean ± SD.

See also Figure S5 and Table S1.

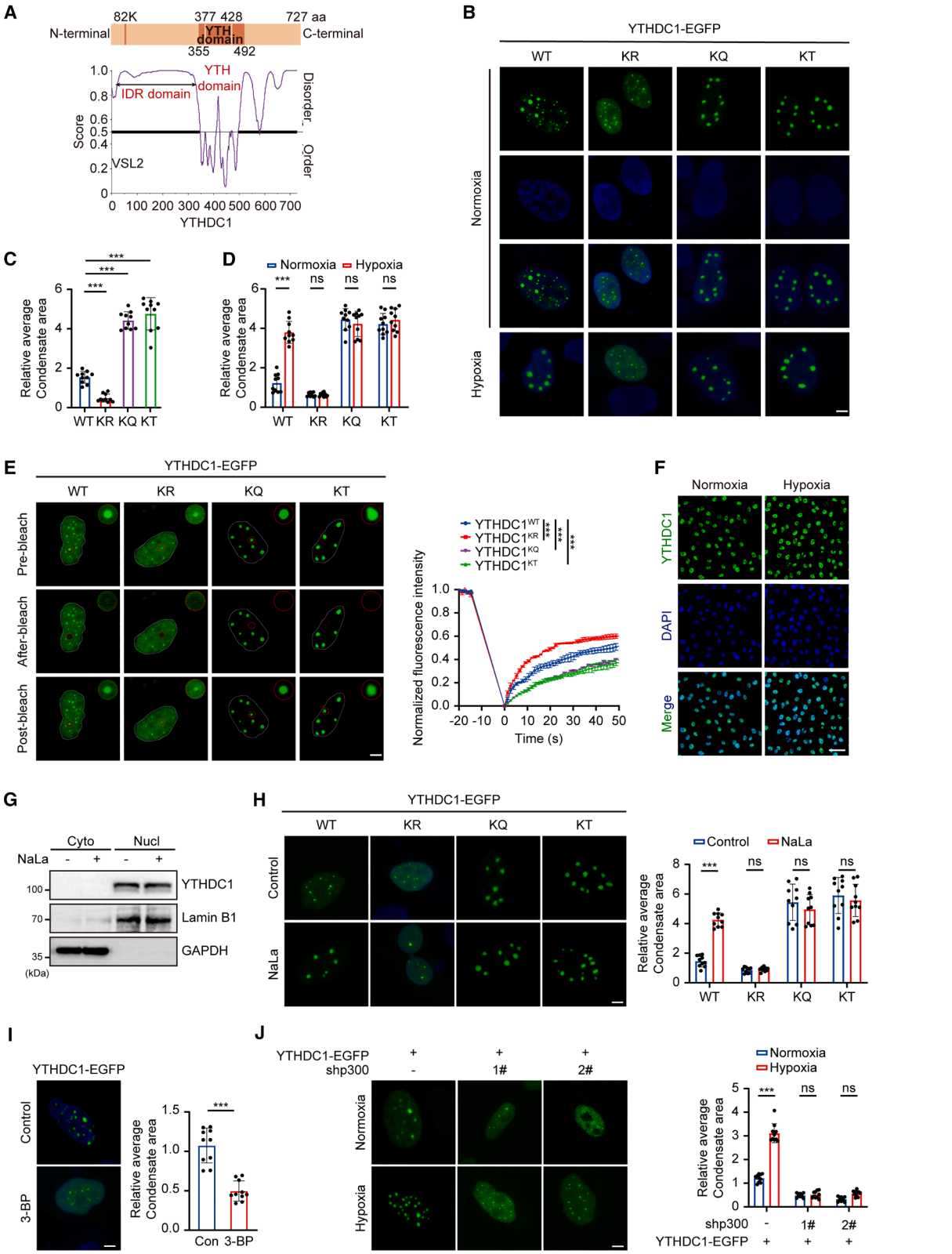

(legend on next page)

an RNA-recognition YTH domain and two IDRs, with the K82 residue located in the N-terminal IDR (Figure 4A). Inspired by this, we wonder if there is a preferred region for Kla. The results showed that 46 (93%) differentially lactylated sites in different proteins were located within the IDRs (Figure S6). This highlights the potential widespread regulation of IDRs by hypoxia-induced lactylation.

IDRs can drive condensate formation via LLPS to influence chromatin regulation, gene expression, and cellular fate.[26] Furthermore, upon detection of endogenous YTHDC1 lactylated at K82 using IF, separate puncta, rather than a diffused status, were observed in cells overexpressing p300 (Figure 2M), indicating that YTHDC1 lactylation mediated by p300 may modulate the nuclear condensates of YTHDC1. Hence, we observed the impact of YTHDC1 lactylation on nuclear condensates in cells. Compared with the YTHDC1^{WT}, condensates were visibly enlarged with clearer edges, and the dynamics detected by fluorescence recovery after photobleaching (FRAP) were slower in YTHDC1^{KQ} (another reported lactylation mimic)[41] and YTHDC1^{KT} groups (Figures 4B, 4C, and 4E). Hypoxia-induced lactylation only altered the condensation of YTHDC1^{WT} but not YTHDC1^{MUT} (Figures 4B lower and 4D). Meanwhile, protein localization of YTHDC1 was not influenced by hypoxia and NaLa treatment (Figures 4F and 4G). In addition, NaLa and 3-BP were introduced to modulate Kla levels in YTHDC1^{WT}. The NaLa group exhibited larger condensates with clearer edges, while 3-BP disrupted YTHDC1 condensates, leading to a significant reduction in the size of condensates (Figures 4H and 4I). After the ablation of p300, hypoxia could no longer enlarge condensates area in cells (Figure 4J). In conclusion, IDR lactylation may influence the condensation of YTHDC1, thereby affecting the malignancy of RCC.

YTHDC1^{K82} lactylation regulates the expression of *E2F2* and *BCL2* mRNAs

To understand the molecular basis for YTHDC1$^{WT/KT}$ condensates impacting RCC progression, we performed RNA sequencing (RNA-seq) on ACHN-YTHDC1$^{WT/KT}$ cells. Substantial expression changes were identified, encompassing 280 downregulated genes and 319 upregulated genes (Figures 5A and 5B). These genes were enriched in the p53 signaling pathway, cell cycle, etc. (Figure 5C). Of which, the upregulated genes, including *BCL2* and *E2F2*, were enriched in cell cycle, p53 signaling pathway, etc. (Figure S7A). While the downregulated genes, including *BAX* and *TP53I3*, were enriched in the p53 signaling pathway, transcriptional misregulation in cancer, etc. (Figure S7B). Subsequently, validation of alterations in the gene expression was performed in ACHN cells (Figure 5D). The results suggest that YTHDC1^{K82la} may regulate the expression of genes governing cell growth, migration, and apoptosis.

We further used RNA immunoprecipitation (RIP)-seq to identify mRNAs targeted by YTHDC1. Results revealed an enrichment of the YTHDC1 m6A binding spectrum in the coding sequence (CDS), with the predominant motif identified as GGAC (Figures 5E and 5F). 1,198 mRNAs were found to bind to YTHDC1 by RIP-seq. Intersection with differentially expressed mRNAs from RNA-seq showed 50 common genes, and the top 20 mRNAs included well-known oncogenes such as *BCL2* and *E2F2* (Figure 5G). Additionally, RIP-reverse-transcription-PCR (RT-PCR), RIP-real-time PCR, and cross-linking immunoprecipitation (CLIP)-real-time PCR results validated that *E2F2* and *BCL2* were indeed the targets of YTHDC1 (Figures 5H, 5I, and S7C). Co-localization of *BCL2* mRNA (fluorescence *in situ* hybridization [FISH]) and the YTHDC1 puncta (IF) in the nucleus also showed that YTHDC1 condensates bound with specific target mRNA (Figure 5J). As YTHDC1 functions as an m6A reader, we also performed methylated RNA immunoprecipitation (MeRIP)-real-time PCR, confirming that the transcripts of *BCL2* and *E2F2* undergo m6A modification and bind to YTHDC1 (Figure S7D).

YTHDC1 can modulate transcriptional activity by regulating chromatin accessibility.[42,43] Hence, we detected the nascent transcript levels of *MYC*, *E2F2*, and *BCL2* under YTHDC1^{K82} lactylation. We found that nascent transcripts remained unaffected by YTHDC1^{K82la} (Figure S7E). This suggests that YTHDC1^{K82la} may regulate the expression abundance of target genes via post-transcriptional mechanisms. Interestingly, YTHDC1^{K82la} enhanced its binding and colocalization with the transcripts of *BCL2* and *E2F2* (Figures 5K–5M, S7F, and S7G) but did not affect the m6A modification levels of *BCL2* and *E2F2* transcripts

Figure 4. Lactylation enlarges YTHDC1 nuclear condensates

(A) Top: structural scheme of YTHDC1, 355–492 is the YTH domain, and 377 and 428 are the key residues. Bottom: graphs plotting intrinsic disorder region for YTHDC1. Predictor of Natural Disordered Regions (PONDR) variable short linear motif predictor version 2 (VSL2) scores are shown on the *y* axis, and amino acid positions are shown on the *x* axis.

(B–D) Live imaging of ACHN cells expressing EGFP-fused YTHDC1 WT and mutants as indicated (B), relative average condensate area under normoxia (C) and hypoxia (D). Scale bar, 5 μm.

(E) Left: representative images of FRAP for YTHDC1 mutant-transfected ACHN cells. Scale bar, 5 μm. Right: quantitative data for fluorescence recovery.

(F) IF analysis indicated that hypoxia treatment does not alter the localization of YTHDC1. Green: YTHDC1, blue: DAPI. Scale bar, 50 μm.

(G) WB indicated that NaLa treatment does not alter the localization of YTHDC1. Lamin B1: nuclear marker; GAPDH: cytoplasmic marker; cyto: cytoplasm; nucl: nucleus.

(H) Left: live imaging of ACHN cells expressing EGFP-fused YTHDC1$^{WT/KR/KT/KQ}$ and treated with/out NaLa. Right: relative average condensate area. Scale bar, 5 μm.

(I) Left: live imaging of ACHN cells expressing EGFP-fused YTHDC1 and treated with/out 3-BP. Right: relative average condensate area. Scale bar, 5 μm.

(J) Left: additional hypoxia treatment failed to increase the area of the YTHDC1 condensates following p300 ablation. Right: relative average condensate area. Scale bar, 5 μm.

Analyses were performed using one-way ANOVA (C), unpaired Student's t test (D and H–J), and two-way ANOVA (E). ***$p < 0.001$, ns: not significant. Data are shown as mean ± SD.

See also Figure S6.

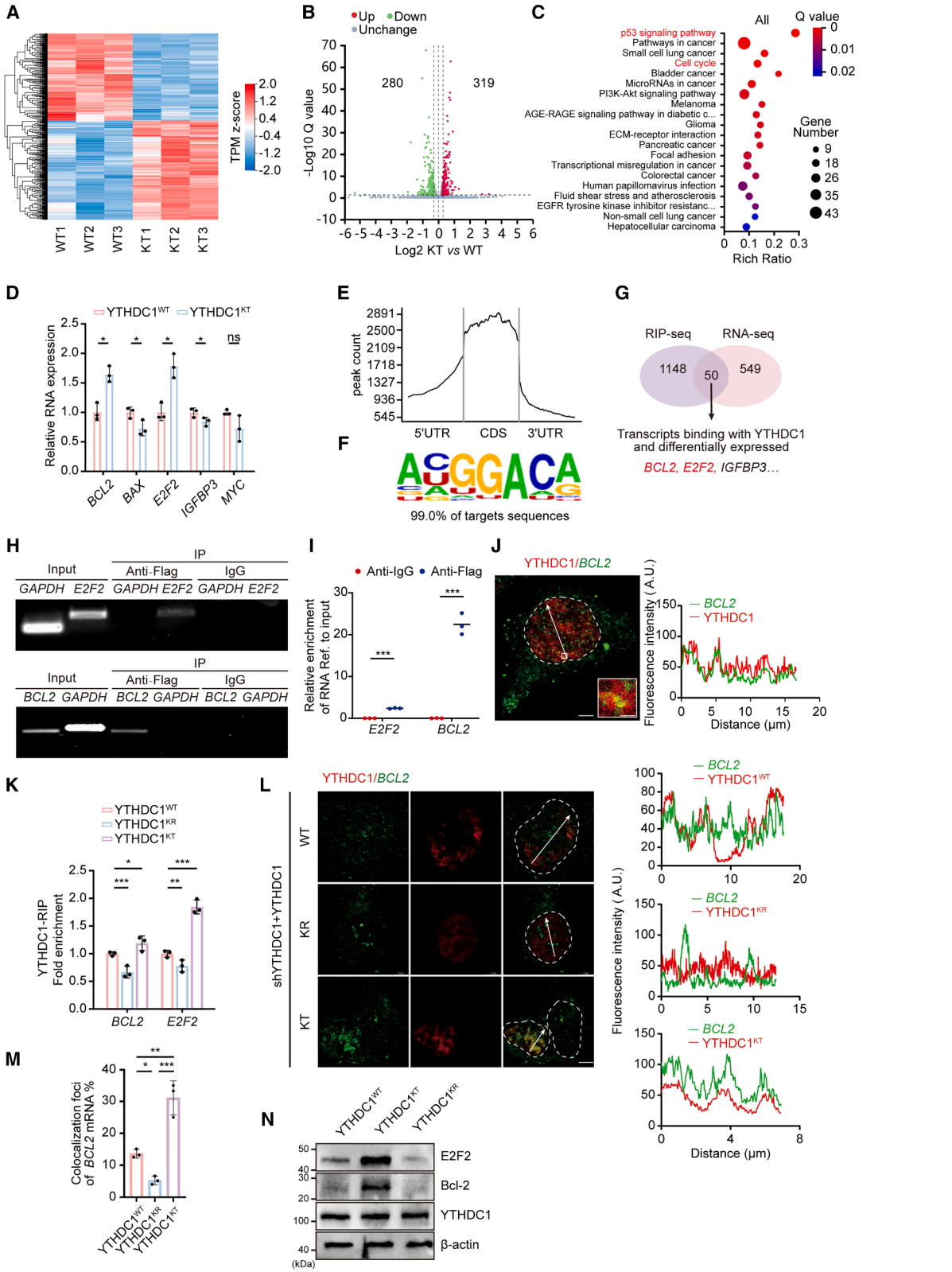

(legend on next page)

(Figure S7H). These results suggest that YTHDC1^{K82la} may regulate gene expression by binding to these transcripts. Furthermore, the protein levels of Bcl-2 and E2F2, like their mRNA levels, were increased in hyperlac-YTHDC1 cells (Figures 5N: YTHDC1^{KT} vs. YTHDC1$^{WT/KR}$ and S7I: NaLa vs. no/3-BP treatment).

YTHDC1^{K82} lactylation promotes RCC progression via protecting target mRNAs from degradation

YTHDC1 may switch post-transcriptional RNA processes, including alternative splicing, RNA decay, and nuclear export, thereby influencing RNA levels.[25,37,38] We found that YTHDC1^{K82la} increased the stabilities of *BCL2* and *E2F2* transcripts (Figure 6A). Poly A-tail exosome targeting (PAXT)-exosome complex targets mRNA for degradation in the cell nucleus, and its core component contains PABPN1.[44] Thus, we tested if condensation protected target mRNAs from the PAXT complex-mediated degradation after YTHDC1 lactylation. Fluorescence results proved that mRNA colocalization with PABPN1 was reduced in the YTHDC1^{KT} group, and conversely, YTHDC1^{KR} increased the colocalization (Figures 6B and 6C). After knocking down PABPN1, YTHDC1 protein levels were not affected (Figures S7J and S7K), while the mRNA levels of *BCL2* and *E2F2* remained unchanged in YTHDC1^{KT} cells in contrast to the increase in YTHDC1^{WT} and YTHDC1^{KR} cells (Figure 6D). These data suggest that YTHDC1^{K82la} may protect *BCL2* and *E2F2* mRNAs from degradation by enhanced condensation.

YTHDC1 is also a crucial factor in promoting mRNA export.[37] Therefore, we also observed the nucleocytoplasmic distribution of *BCL2*. Although RNA-FISH and real-time PCR results showed an increase of *BCL2* mRNA in both the nucleus and cytoplasm of YTHDC1^{KT} cells, the nuclear-cytoplasmic ratio remained unchanged (Figures 6E–6G). This suggests that YTHDC1^{K82la} does not regulate the expression via mRNA export.

Based on these data and the known roles of Bcl-2 and E2F2 in tumor progression, we further investigated the impact of Bcl-2 and E2F2 on YTHDC1^{K82la}-mediated RCC progression. The results revealed that E2F2 overexpression partially reversed the cell cycle arrest and malignancy suppression in YTHDC1^{KR} cells (Figures 6H–6K), suggesting that YTHDC1^{K82la}-mediated tumor progression required E2F2. Furthermore, the cells overexpressing YTHDC1^{KR} show a higher proportion of apoptosis responding to sunitinib, and the overexpression of Bcl-2 largely restored the apoptosis tolerance of YTHDC1^{KR} cells to sunitinib (Figure 6L). This suggests that YTHDC1^{K82la}, which mediates tumor promotion, may be the therapeutic target for RCC clinical application. Overall, our results emphasize the importance of targeting the YTHDC1^{K82la}-phase separation-*BCL2* and *E2F2* axis in RCC.

DISCUSSION

In this study, a comprehensive landscape of hypoxia-regulated lactylome in RCC was depicted. Subsequently, key lactylated protein and site (YTHDC1^{K82}) under hypoxia were identified. Here, we propose a potential model in which YTHDC1^{K82la} promoted RCC progression by enlarging the condensates to protect target mRNAs *BCL2* and *E2F2* from degradation (Figure 6M). By elaborating on YTHDC1 lactylation-regulated phase-separated condensates and RNA-binding capacity, we provide mechanistic insights into the regulation of hypoxia-promoted YTHDC1 lactylation on RCC progression. Inhibiting lactylation might be a promising therapeutic strategy for RCC.

Partial RCCs are characterized by *VHL* mutation, and *VHL* mutation-induced pseudo-hypoxia impacts histone lactylation levels and ccRCC progression.[23] However, HIF1α gene loss occurs in some RCC cell lines harboring *VHL* mutations.[45] This reminds us that *VHL* mutation-HIF1α upregulation might not be the only mechanism for lactylation in RCC. Our study has observed that hypoxia promotes lactylation also through a HIF-independent mechanism. The underlying mechanism remains unclear and is worthy of investigation.

PTMs of IDRs, such as acetylation, O-GlcNAcylation, and phosphorylation, spatiotemporally regulate protein condensation and impact membraneless organelle formation *in vivo*.[35,46,47]

Figure 5. YTHDC1^{K82la} regulates the expression of *E2F2* and *BCL2* mRNAs

(A) Heatmap of 599 differentially expressed genes (DEGs) from RNA-seq analyses of ACHN-shYTHDC1-YTHDC1^{WT} and ACHN-shYTHDC1-YTHDC1^{KT} cells ($n = 3$) ($p < 0.05$, fold change > 1.2).

(B) Volcano plot showing DEGs in ACHN-shYTHDC1-YTHDC1^{KT} vs. ACHN-shYTHDC1-YTHDC1^{WT} cells. The vertical and horizontal dashed lines denote the cutoff values (−0.26, 0.26) for $\log_2$ (KT/WT ratio) and p value (<0.05), respectively.

(C) Bubble plot showing pathways enriched by DEGs of KT/WT cells.

(D) Real-time PCR validation of differential expression of the selected target genes in ACHN-shYTHDC1-YTHDC1^{WT} and ACHN-shYTHDC1-YTHDC1^{KT} cells.

(E) Distribution of RIP peak counts of ACHN-shYTHDC1-YTHDC1^{WT} mRNA. CDS, coding sequence.

(F) Binding motif of ACHN-shYTHDC1-YTHDC1^{WT}.

(G) Intersection of RNA- and RIP-seq data to define target genes regulated by YTHDC1 lactylation.

(H and I) YTHDC1-RIP analyses showing YTHDC1 enrichments at mRNAs of the selected target genes in ACHN cells. RT-PCR (H), real-time PCR (I).

(J) Left: representative image of *BCL2* mRNAs (green) by FISH and YTHDC1 (red) by IF in ACHN. Scale bar, 5 μm. Right: quantification of the fluorescence intensity along the line embedded in the zoomed-in images following the arrow direction.

(K) YTHDC1-RIP analysis of YTHDC1 enrichments at mRNAs of *BCL2* and *E2F2* in ACHN-shYTHDC1-YTHDC1$^{WT/KR/KT}$ cells.

(L) Left: representative image of *BCL2* mRNAs (green) by FISH and YTHDC1 (red) by IF in ACHN-shYTHDC1-YTHDC1$^{WT/KR/KT}$ cells. Scale bar, 5 μm. Right: quantification of the fluorescence intensity along the line embedded in the zoomed-in images following the arrow direction.

(M) Quantitation of colocalization of *BCL2* mRNAs with YTHDC1 protein.

(N) The protein levels of Bcl-2 and E2F2 in ACHN-shYTHDC1-YTHDC1$^{WT/KR/KT}$ cells were detected by WB.

Analyses were performed using unpaired two-tailed Student's t test (D and I) and one-way ANOVA (K and M). $^*p < 0.05$, $^{**}p < 0.01$, $^{***}p < 0.001$, ns: not significant. Data are shown as means ± SD.

See also Figure S7.

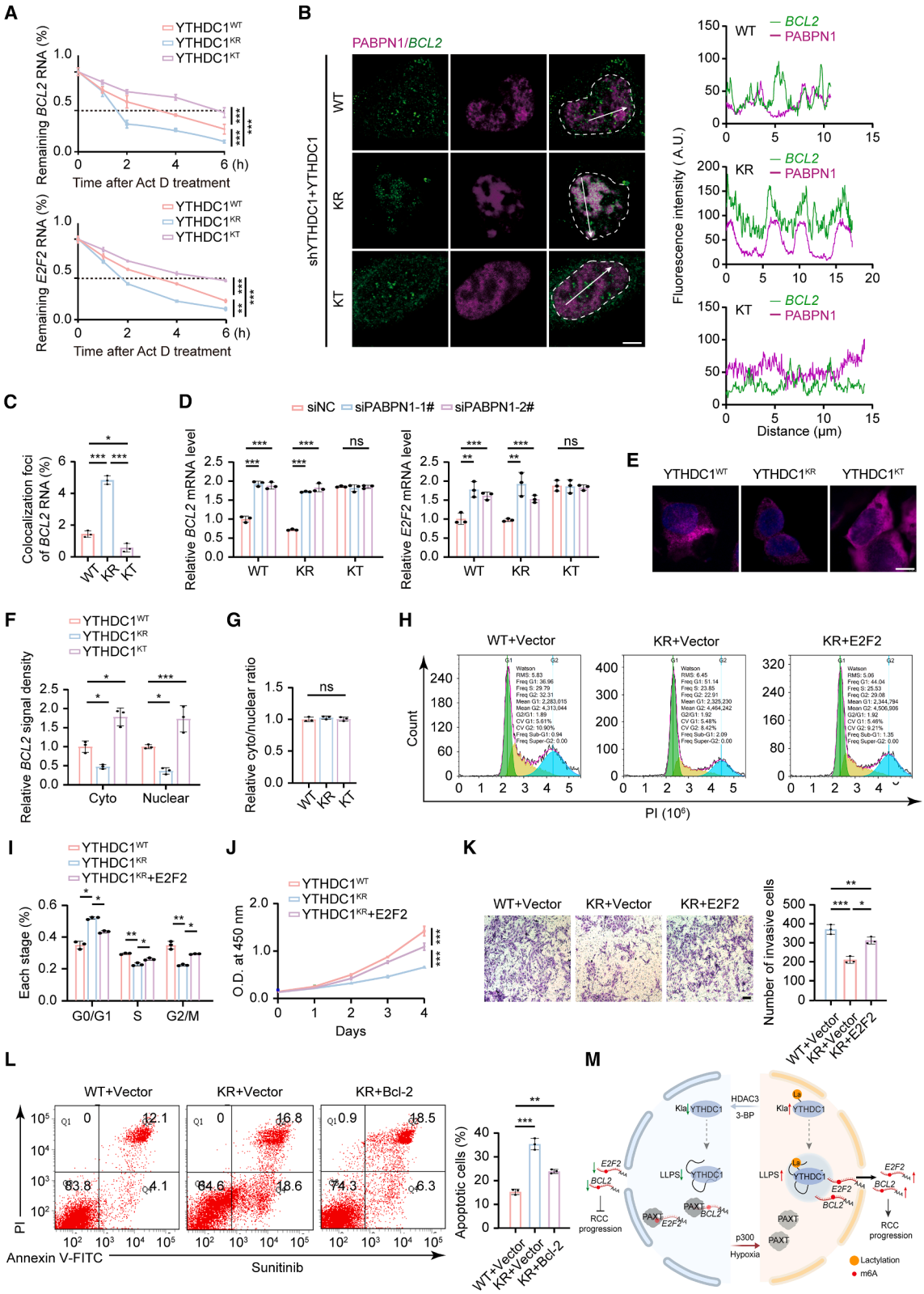

(legend on next page)

For example, deacetylation of HP1γ at the K5 affects the nuclear condensation of HP1γ and promotes multiple myeloma drug resistance.[48] The N-terminal IDR acetylation of DDX3X impairs the formation of liquid droplets.[46] In this study, we showed that lactylation of YTHDC1^{K82} affected the nuclear condensation of YTHDC1 in RCC cells. p300, acting as a lactyltransferase, interacts with YTHDC1 and augments the condensation. YTHDC1^{K82la} shields *BCL2* and *E2F2* from degradation by the PAXT-exosome complex through phase separation. We speculate that under hypoxic stress, nuclear YTHDC1 rapidly senses metabolic changes and undergoes lactylation, forming phase-separated compartments that proactively shield nuclear *BCL2* mRNAs from PAXT-mediated decay. Whether distinct mRNAs are protected by alternative decay-avoidance mechanisms remains to be explored in future studies. Notably, the IDRs of RBPs can modulate RNA binding by altering protein conformation, a process that can be regulated by PTMs.[49–52] Here, lactylation at the K82 residue within the IDR domain impacts the binding of YTHDC1 to RNA. The deeper mechanism merits further investigation. In summary, our observations provide a mechanistic insight into how RBPs bridge lactylation to phase separation and thereby promote the progression of RCC.

Another interesting finding is that most differential lactylation sites are located in IDRs. In comparison, acetylation is often found in regions with ordered secondary structure.[53] This suggests that lactylation and acetylation prefer different protein regions for modification. IDRs play a crucial role in mediating phase separation and the formation of biomolecular condensates.[26] That higher proportion of lactylation sites located in IDRs also suggests that lactylation may more easily affect LLPS. In all, our study points out the potential connection between lactylation-IDR-phase separation.

In summary, this study elucidates that YTHDC1^{K82la} induces the expansion of nuclear condensates and sequesters *BCL2* and *E2F2*, thereby protecting them from degradation by the PAXT-exosome complex. This presents the precise spatial and temporal protein regulation in living cells. These results successfully link the chain of events involving Kla—phase-separated condensates of RBPs—RCC progression. This study also provides a theoretical basis and perspective for the therapeutic regulation of Kla and phase separation in cancer treatment.

Limitations of the study

We found a HIF-independent pathway exerts a role in hypoxia-induced lactylation in RCC cell lines; however, the precise mechanism remains to be further explored.

While our results suggest that YTHDC1 lactylation influences condensation and boosts its RNA-binding capacity, the presence of extensive IDRs renders existing techniques inadequate for accurately determining the impact of lactylation on the spatial structure of YTHDC1. The exact mechanism and structural details of this modification remain elusive. Additionally, more advanced techniques, such as third-generation sequencing and hybridization chain reaction (HCR)-FISH, are needed to accurately and quantitatively characterize the role of YTHDC1 condensates in RNA splicing patterns and RNA stability, respectively.

Due to methodological limitations, point mutations at the YTHDC1^{K82}, although useful, may introduce other PTMs at the same site. More precise tools and methods need to be developed to address these challenges in the future.

RESOURCE AVAILABILITY

Lead contact

Further information and requests for resources and reagents should be directed to and will be fulfilled by the lead contact, Junfang Zheng (zhengjf@ccmu.edu.cn).

Materials availability

All materials generated in this study are available from the lead contact with a completed materials transfer agreement.

Data and code availability

- The mass spectrometry proteomics data were deposited to the ProteomeXchange Consortium via the PRIDE partner repository with the dataset. The raw data from RNA-seq and RIP-seq were submitted to the NCBI Sequence Read Archive (SRA) database. Unprocessed images are deposited at Mendeley. Accession numbers are listed in the key resources table, and all deposited data will be publicly available upon publication.
- This paper does not report original code.
- Any additional information required to reanalyze the data reported in this paper is available from the lead contact upon request.

Figure 6. YTHDC1^{K82la} promotes RCC progression via protecting target mRNAs from degradation

(A) The mRNA half-life time (t1/2) of *BCL2* and *E2F2* transcripts in ACHN-shYTHDC1-YTHDC1$^{WT/KR/KT}$ cells.

(B) Left: representative image of *BCL2* mRNAs (green) by FISH and PABPN1 (magenta) by IF in ACHN-shYTHDC1-YTHDC1$^{WT/KR/KT}$ cells. Scale bar, 5 μm. Right: quantification of the fluorescence intensity along the line embedded in the zoomed-in images following the arrow direction.

(C) Quantitation of colocalization of *BCL2* mRNAs with PABPN1 protein.

(D) The effect of knocking down PABPN1, the core component of the PAXT complex, on *BCL2* and *E2F2* mRNAs in ACHN-YTHDC1$^{WT/KR/KT}$ cells.

(E) Images of *BCL2* mRNA (magenta) by FISH in ACHN-shYTHDC1-YTHDC1$^{WT/KR/KT}$ cells. Scale bar, 5 μm.

(F) Relative *BCL2* signal density in the nucleus and cytoplasm.

(G) Relative cyto/nuclear ratio of *BCL2* mRNA by real-time PCR analysis in ACHN-shYTHDC1-YTHDC1$^{WT/KR/KT}$ cells.

(H–K) Cell cycle (flow cytometric analysis) (H and I), proliferation (CCK-8 assay) (J), and invasion (transwell assay) (K) in ACHN-YTHDC1$^{WT/KR}$ cells with/out E2F2 expression. Scale bar, 50 μm.

(L) Left: flow cytometric analysis of apoptosis in ACHN-YTHDC1$^{WT/KR}$ cells with/out BcL-2 expression. Right: statistical results of apoptotic rates.

(M) A proposed model for YTHDC1^{K82la} regulating *BCL2* and *E2F2* mRNAs via phase-separated condensates.

Analyses were performed using two-way ANOVA (A and J) and one-way ANOVA (C, D, F, G, I, K, and L). $^{*}p < 0.05$, $^{**}p < 0.01$, $^{***}p < 0.001$, ns: not significant. Data are shown as mean ± SD.

See also Figure S7.

ACKNOWLEDGMENTS

We thank Prof. Dr. Hongquan Zhang (School of Basic Medical Sciences, Peking University) for the kind gift of the FLAG-HDAC1–9 and HA-p300/CBP/KAT8/KAT2B/KAT5. We thank Prof. Dr. Jianyuan Luo (School of Basic Medical Sciences, Peking University) for the kind gift of the shp300-1#/2# plasmids and for his guidance in this study. We thank the Core Facility Center, Capital Medical University, for providing instrumental support. We also appreciate Dr. Tianhang Qiu from PTM-Bio for his guidance on the lactylome data analysis. This work was supported by the National Natural Science Foundation of China (no. 82172923), the Beijing Nova Program (no. 20230484483), and Innovative Group Cultivation Project for Basic Medicine (no. CX25XT03).

AUTHOR CONTRIBUTIONS

Conceptualization, J.Z., C.D., and Y.T.; methodology, C.D. and Y.T.; validation, C.D. and Y.T.; formal analysis, C.D.; investigation, C.D., Y.T., and H.Y.; visualization, C.D. and H.Y.; data curation, J.Z., C.D., Y.T., and H.Y.; writing – original draft, J.Z., C.D., Y.T., and H.Y.; writing – review and editing, J.Z. and C.D.; funding acquisition, J.Z.; resources, J.Z.; supervision, J.Z.; and project administration, J.Z.

DECLARATION OF INTERESTS

The authors declare no competing interests.

STAR★METHODS

Detailed methods are provided in the online version of this paper and include the following:

- KEY RESOURCES TABLE
- EXPERIMENTAL MODEL AND STUDY PARTICIPANT DETAILS
  - Tissue collection
  - Cell culture and treatment
- METHOD DETAILS
  - Immunofluorescence
  - Western blotting
  - Transfection
  - Virus production and infection
  - EdU assay
  - Colony formation assay
  - Wound healing assay
  - Transwell assay
  - CCK-8 assay
  - Xenograft
  - LC-MS analysis
  - Parallel reaction monitoring
  - Immunoprecipitation
  - Cell cycle analysis
  - Fluorescence recovery after photobleaching
  - Protein purification
  - *In vitro* lactylation assay
  - RNA-seq and RIP-seq
  - RT-PCR
  - RT-qPCR
  - RIP and MeRIP assays
  - Cross-linking immunoprecipitation q-PCR
  - Nascent RNA assay
  - mRNA stability assay
  - Cellular fractionation and RNA isolation
  - RNA-Fluorescence *in situ* hybridization in conjugation with fluorescent immunostaining
  - Apoptosis analysis
- QUANTIFICATION AND STATISTICAL ANALYSIS

SUPPLEMENTAL INFORMATION

Supplemental information can be found online at https://doi.org/10.1016/j.molcel.2025.06.017.

Received: May 15, 2024
Revised: December 13, 2024
Accepted: June 19, 2025
Published: July 17, 2025

REFERENCES

1. Li, X., Yang, Y., Zhang, B., Lin, X., Fu, X., An, Y., Zou, Y., Wang, J.X., Wang, Z., and Yu, T. (2022). Lactate metabolism in human health and disease. Signal Transduct. Target. Ther. *7*, 305. https://doi.org/10.1038/s41392-022-01151-3.
2. Zhang, D., Tang, Z., Huang, H., Zhou, G., Cui, C., Weng, Y., Liu, W., Kim, S., Lee, S., Perez-Neut, M., et al. (2019). Metabolic regulation of gene expression by histone lactylation. Nature *574*, 575–580. https://doi.org/10.1038/s41586-019-1678-1.
3. Yang, K., Fan, M., Wang, X., Xu, J., Wang, Y., Tu, F., Gill, P.S., Ha, T., Liu, L., Williams, D.L., et al. (2022). Lactate promotes macrophage HMGB1 lactylation, acetylation, and exosomal release in polymicrobial sepsis. Cell Death Differ. *29*, 133–146. https://doi.org/10.1038/s41418-021-00841-9.
4. Chen, H., Li, Y., Li, H., Chen, X., Fu, H., Mao, D., Chen, W., Lan, L., Wang, C., Hu, K., et al. (2024). NBS1 lactylation is required for efficient DNA repair and chemotherapy resistance. Nature *631*, 663–669. https://doi.org/10.1038/s41586-024-07620-9.
5. Xie, B., Zhang, M., Li, J., Cui, J., Zhang, P., Liu, F., Wu, Y., Deng, W., Ma, J., Li, X., et al. (2024). KAT8-catalyzed lactylation promotes eEF1A2-mediated protein synthesis and colorectal carcinogenesis. Proc. Natl. Acad. Sci. USA *121*, e2314128121. https://doi.org/10.1073/pnas.2314128121.
6. Niu, Z., Chen, C., Wang, S., Lu, C., Wu, Z., Wang, A., Mo, J., Zhang, J., Han, Y., Yuan, Y., et al. (2024). HBO1 catalyzes lysine lactylation and mediates histone H3K9la to regulate gene transcription. Nat. Commun. *15*, 3561. https://doi.org/10.1038/s41467-024-47900-6.
7. Moreno-Yruela, C., Zhang, D., Wei, W., Bæk, M., Liu, W., Gao, J., Danková, D., Nielsen, A.L., Bolding, J.E., Yang, L., et al. (2022). Class I histone deacetylases (HDAC1-3) are histone lysine delactylases. Sci. Adv. *8*, eabi6696. https://doi.org/10.1126/sciadv.abi6696.
8. Zong, Z., Xie, F., Wang, S., Wu, X., Zhang, Z., Yang, B., and Zhou, F. (2024). Alanyl-tRNA synthetase, AARS1, is a lactate sensor and lactyltransferase that lactylates p53 and contributes to tumorigenesis. Cell *187*, 2375–2392.e33. https://doi.org/10.1016/j.cell.2024.04.002.
9. Li, H., Liu, C., Li, R., Zhou, L., Ran, Y., Yang, Q., Huang, H., Lu, H., Song, H., Yang, B., et al. (2024). AARS1 and AARS2 sense L-lactate to regulate cGAS as global lysine lactyltransferases. Nature *634*, 1229–1237. https://doi.org/10.1038/s41586-024-07992-y.
10. Yu, J., Chai, P., Xie, M., Ge, S., Ruan, J., Fan, X., and Jia, R. (2021). Histone lactylation drives oncogenesis by facilitating m(6)A reader protein YTHDF2 expression in ocular melanoma. Genome Biol. *22*, 85. https://doi.org/10.1186/s13059-021-02308-z.
11. Gu, X., Zhuang, A., Yu, J., Yang, L., Ge, S., Ruan, J., Jia, R., Fan, X., and Chai, P. (2024). Histone lactylation-boosted ALKBH3 potentiates tumor progression and diminished promyelocytic leukemia protein nuclear condensates by m1A demethylation of SP100A. Nucleic Acids Res. *52*, 2273–2289. https://doi.org/10.1093/nar/gkad1193.
12. Cai, J., Song, L., Zhang, F., Wu, S., Zhu, G., Zhang, P., Chen, S., Du, J., Wang, B., Cai, Y., et al. (2024). Targeting SRSF10 might inhibit M2 macrophage polarization and potentiate anti-PD-1 therapy in hepatocellular carcinoma. Cancer Commun. (Lond.) *44*, 1231–1260. https://doi.org/10.1002/cac2.12607.

13. Merkuri, F., Rothstein, M., and Simoes-Costa, M. (2024). Histone lactylation couples cellular metabolism with developmental gene regulatory networks. Nat. Commun. *15*, 90. https://doi.org/10.1038/s41467-023-44121-1.

14. Yang, Z., Zheng, Y., and Gao, Q. (2024). Lysine lactylation in the regulation of tumor biology. Trends Endocrinol. Metab. *35*, 720–731. https://doi.org/10.1016/j.tem.2024.01.011.

15. Gao, X., Pang, C., Fan, Z., Wang, Y., Duan, Y., and Zhan, H. (2024). Regulation of newly identified lysine lactylation in cancer. Cancer Lett. *587*, 216680. https://doi.org/10.1016/j.canlet.2024.216680.

16. Chen, Y., Wu, J., Zhai, L., Zhang, T., Yin, H., Gao, H., Zhao, F., Wang, Z., Yang, X., Jin, M., et al. (2024). Metabolic regulation of homologous recombination repair by MRE11 lactylation. Cell *187*, 294–311.e21. https://doi.org/10.1016/j.cell.2023.11.022.

17. Sun, L., Zhang, Y., Yang, B., Sun, S., Zhang, P., Luo, Z., Feng, T., Cui, Z., Zhu, T., Li, Y., et al. (2023). Lactylation of METTL16 promotes cuproptosis via m(6)A-modification on FDX1 mRNA in gastric cancer. Nat. Commun. *14*, 6523. https://doi.org/10.1038/s41467-023-42025-8.

18. Raychaudhuri, D., Singh, P., Chakraborty, B., Hennessey, M., Tannir, A.J., Byregowda, S., Natarajan, S.M., Trujillo-Ocampo, A., Im, J.S., and Goswami, S. (2024). Histone lactylation drives CD8(+) T cell metabolism and function. Nat. Immunol. *25*, 2140–2151. https://doi.org/10.1038/s41590-024-01985-9.

19. Thompson, J.A., Schneider, B.J., Brahmer, J., Achufusi, A., Armand, P., Berkenstock, M.K., Bhatia, S., Budde, L.E., Chokshi, S., Davies, M., et al. (2022). Management of Immunotherapy-Related Toxicities, Version 1.2022, NCCN Clinical Practice Guidelines in Oncology. J. Natl. Compr. Canc. Netw. *20*, 387–405. https://doi.org/10.6004/jnccn.2022.0020.

20. Kim, I.H., and Lee, H.J. (2022). The Frontline Immunotherapy-Based Treatment of Advanced Clear Cell Renal Cell Carcinoma: Current Evidence and Clinical Perspective. Biomedicines *10*, 251. https://doi.org/10.3390/biomedicines10020251.

21. Barata, P.C., and Rini, B.I. (2017). Treatment of renal cell carcinoma: Current status and future directions. CA Cancer J. Clin. *67*, 507–524. https://doi.org/10.3322/caac.21411.

22. Lai, Y., Tang, F., Huang, Y., He, C., Chen, C., Zhao, J., Wu, W., and He, Z. (2021). The tumour microenvironment and metabolism in renal cell carcinoma targeted or immune therapy. J. Cell. Physiol. *236*, 1616–1627. https://doi.org/10.1002/jcp.29969.

23. Yang, J., Luo, L., Zhao, C., Li, X., Wang, Z., Zeng, Z., Yang, X., Zheng, X., Jie, H., Kang, L., et al. (2022). A Positive Feedback Loop between Inactive VHL-Triggered Histone Lactylation and PDGFRbeta Signaling Drives Clear Cell Renal Cell Carcinoma Progression. Int. J. Biol. Sci. *18*, 3470–3483. https://doi.org/10.7150/ijbs.73398.

24. Xu, C., Wang, X., Liu, K., Roundtree, I.A., Tempel, W., Li, Y., Lu, Z., He, C., and Min, J. (2014). Structural basis for selective binding of m6A RNA by the YTHDC1 YTH domain. Nat. Chem. Biol. *10*, 927–929. https://doi.org/10.1038/nchembio.1654.

25. Cheng, Y., Xie, W., Pickering, B.F., Chu, K.L., Savino, A.M., Yang, X., Luo, H., Nguyen, D.T., Mo, S., Barin, E., et al. (2021). N(6)-Methyladenosine on mRNA facilitates a phase-separated nuclear body that suppresses myeloid leukemic differentiation. Cancer Cell *39*, 958–972.e8. https://doi.org/10.1016/j.ccell.2021.04.017.

26. Ahn, J.H., Davis, E.S., Daugird, T.A., Zhao, S., Quiroga, I.Y., Uryu, H., Li, J., Storey, A.J., Tsai, Y.H., Keeley, D.P., et al. (2021). Phase separation drives aberrant chromatin looping and cancer development. Nature *595*, 591–595. https://doi.org/10.1038/s41586-021-03662-5.

27. Trojanowski, J., Frank, L., Rademacher, A., Mücke, N., Grigaitis, P., and Rippe, K. (2022). Transcription activation is enhanced by multivalent interactions independent of phase separation. Mol. Cell *82*, 1878–1893.e10. https://doi.org/10.1016/j.molcel.2022.04.017.

28. Shen, H., Yanas, A., Owens, M.C., Zhang, C., Fritsch, C., Fare, C.M., Copley, K.E., Shorter, J., Goldman, Y.E., and Liu, K.F. (2022). Sexually dimorphic RNA helicases DDX3X and DDX3Y differentially regulate RNA metabolism through phase separation. Mol. Cell *82*, 2588–2603.e9. https://doi.org/10.1016/j.molcel.2022.04.022.

29. Wei, M., Huang, X., Liao, L., Tian, Y., and Zheng, X. (2023). SENP1 Decreases RNF168 Phase Separation to Promote DNA Damage Repair and Drug Resistance in Colon Cancer. Cancer Res. *83*, 2908–2923. https://doi.org/10.1158/0008-5472.CAN-22-4017.

30. Lu, Y., Gan, L., Di, S., Nie, F., Shi, H., Wang, R., Yang, F., Qin, W., and Wen, W. (2024). The role of phase separation in RNA modification: both cause and effect. Int. J. Biol. Macromol. *280*, 135907. https://doi.org/10.1016/j.ijbiomac.2024.135907.

31. Dai, C., Cao, J., Tang, Y., Jiang, Y., Luo, C., and Zheng, J. (2024). YTHDF3 phase separation regulates HSPA13-dependent clear cell renal cell carcinoma development and immune evasion. Cancer Sci. *115*, 2588–2601. https://doi.org/10.1111/cas.16228.

32. Zhang, J., Ni, Z., Zhang, Y., Guo, Y., Zhai, R., Wang, M., Gong, Z., Wang, M., Zeng, F., Gu, Z., et al. (2024). DAZAP1 Phase Separation Regulates Mitochondrial Metabolism to Facilitate Invasion and Metastasis of Oral Squamous Cell Carcinoma. Cancer Res. *84*, 3818–3833. https://doi.org/10.1158/0008-5472.CAN-24-0067.

33. Mehta, S., and Zhang, J. (2022). Liquid-liquid phase separation drives cellular function and dysfunction in cancer. Nat. Rev. Cancer *22*, 239–252. https://doi.org/10.1038/s41568-022-00444-7.

34. Shin, Y., and Brangwynne, C.P. (2017). Liquid phase condensation in cell physiology and disease. Science *357*, eaaf4382. https://doi.org/10.1126/science.aaf4382.

35. Chen, Y., Wan, R., Zou, Z., Lao, L., Shao, G., Zheng, Y., Tang, L., Yuan, Y., Ge, Y., He, C., et al. (2023). O-GlcNAcylation determines the translational regulation and phase separation of YTHDF proteins. Nat. Cell Biol. *25*, 1676–1690. https://doi.org/10.1038/s41556-023-01258-x.

36. Bhandari, V., Hoey, C., Liu, L.Y., Lalonde, E., Ray, J., Livingstone, J., Lesurf, R., Shiah, Y.J., Vujcic, T., Huang, X., et al. (2019). Molecular landmarks of tumor hypoxia across cancer types. Nat. Genet. *51*, 308–318. https://doi.org/10.1038/s41588-018-0318-2.

37. Roundtree, I.A., Luo, G.Z., Zhang, Z., Wang, X., Zhou, T., Cui, Y., Sha, J., Huang, X., Guerrero, L., Xie, P., et al. (2017). YTHDC1 mediates nuclear export of N(6)-methyladenosine methylated mRNAs. eLife *6*, e31311. https://doi.org/10.7554/eLife.31311.

38. Xiao, W., Adhikari, S., Dahal, U., Chen, Y.S., Hao, Y.J., Sun, B.F., Sun, H.Y., Li, A., Ping, X.L., Lai, W.Y., et al. (2016). Nuclear m(6)A Reader YTHDC1 Regulates mRNA Splicing. Mol. Cell *61*, 507–519. https://doi.org/10.1016/j.molcel.2016.01.012.

39. Sheng, Y., Wei, J., Yu, F., Xu, H., Yu, C., Wu, Q., Liu, Y., Li, L., Cui, X.L., Gu, X., et al. (2021). A critical role of nuclear m6A reader YTHDC1 in leukemogenesis by regulating MCM complex-mediated DNA replication. Blood *138*, 2838–2852. https://doi.org/10.1182/blood.2021011707.

40. Duan, Y., Zhan, H., Wang, Q., Li, B., Gao, H., Liu, D., Xu, Q., Gao, X., Liu, Z., Gao, P., et al. (2024). Integrated Lactylome Characterization Reveals the Molecular Dynamics of Protein Regulation in Gastrointestinal Cancers. Adv. Sci. (Weinh) *11*, e2400227. https://doi.org/10.1002/advs.202400227.

41. Jin, J., Bai, L., Wang, D., Ding, W., Cao, Z., Yan, P., Li, Y., Xi, L., Wang, Y., Zheng, X., et al. (2023). SIRT3-dependent delactylation of cyclin E2 prevents hepatocellular carcinoma growth. EMBO Rep. *24*, e56052. https://doi.org/10.15252/embr.202256052.

42. Li, Y., Xia, L., Tan, K., Ye, X., Zuo, Z., Li, M., Xiao, R., Wang, Z., Liu, X., Deng, M., et al. (2020). N(6)-Methyladenosine co-transcriptionally directs the demethylation of histone H3K9me2. Nat. Genet. *52*, 870–877. https://doi.org/10.1038/s41588-020-0677-3.

43. Liu, J., Dou, X., Chen, C., Chen, C., Liu, C., Xu, M.M., Zhao, S., Shen, B., Gao, Y., Han, D., et al. (2020). N6-methyladenosine of chromosome-associated regulatory RNA regulates chromatin state and transcription. Science *367*, 580–586. https://doi.org/10.1126/science.aay6018.

44. Rouvière, J.O., Salerno-Kochan, A., Lykke-Andersen, S., Garland, W., Dou, Y., Rathore, O., Molska, E.Ś., Wu, G., Schmid, M., Bugai, A., et al. (2023). ARS2 instructs early transcription termination-coupled RNA decay by recruiting ZC3H4 to nascent transcripts. Mol. Cell *83*, 2240–2257.e6. https://doi.org/10.1016/j.molcel.2023.05.028.

45. Cho, H., Du, X., Rizzi, J.P., Liberzon, E., Chakraborty, A.A., Gao, W., Carvo, I., Signoretti, S., Bruick, R.K., Josey, J.A., et al. (2016). On-target efficacy of a HIF-2alpha antagonist in preclinical kidney cancer models. Nature *539*, 107–111. https://doi.org/10.1038/nature19795.

46. Saito, M., Hess, D., Eglinger, J., Fritsch, A.W., Kreysing, M., Weinert, B.T., Choudhary, C., and Matthias, P. (2019). Acetylation of intrinsically disordered regions regulates phase separation. Nat. Chem. Biol. *15*, 51–61. https://doi.org/10.1038/s41589-018-0180-7.

47. Wang, D., Sun, T., Xia, Y., Zhao, Z., Sheng, X., Li, S., Ma, Y., Li, M., Su, X., Zhang, F., et al. (2023). Homodimer-mediated phosphorylation of C/EBPalpha-p42 S16 modulates acute myeloid leukaemia differentiation through liquid-liquid phase separation. Nat. Commun. *14*, 6907. https://doi.org/10.1038/s41467-023-42650-3.

48. Li, X., Wang, S., Xie, Y., Jiang, H., Guo, J., Wang, Y., Peng, Z., Hu, M., Wang, M., Wang, J., et al. (2023). Deacetylation induced nuclear condensation of HP1gamma promotes multiple myeloma drug resistance. Nat. Commun. *14*, 1290. https://doi.org/10.1038/s41467-023-37013-x.

49. Shen, H., Kan, J.L.C., and Green, M.R. (2004). Arginine-serine-rich domains bound at splicing enhancers contact the branchpoint to promote prespliceosome assembly. Mol. Cell *13*, 367–376. https://doi.org/10.1016/s1097-2765(04)00025-5.

50. Ramos, A., Hollingworth, D., and Pastore, A. (2003). G-quartet-dependent recognition between the FMRP RGG box and RNA. RNA *9*, 1198–1207. https://doi.org/10.1261/rna.5960503.

51. Modic, M., Adamek, M., and Ule, J. (2024). The impact of IDR phosphorylation on the RNA binding profiles of proteins. Trends Genet. *40*, 580–586. https://doi.org/10.1016/j.tig.2024.04.004.

52. Qiu, C., Zhang, Z., Wine, R.N., Campbell, Z.T., Zhang, J., and Hall, T.M.T. (2023). Intra- and inter-molecular regulation by intrinsically-disordered regions governs PUF protein RNA binding. Nat. Commun. *14*, 7323. https://doi.org/10.1038/s41467-023-43098-1.

53. Choudhary, C., Kumar, C., Gnad, F., Nielsen, M.L., Rehman, M., Walther, T.C., Olsen, J.V., and Mann, M. (2009). Lysine acetylation targets protein complexes and co-regulates major cellular functions. Science *325*, 834–840. https://doi.org/10.1126/science.1175371.

STAR★METHODS

KEY RESOURCES TABLE

REAGENT or RESOURCE	SOURCE	IDENTIFIER
Antibodies		
Rabbit monoclonal anti-L-Lactyllysine	PTM Bio, China	Cat# PTM-1401RM; RRID: AB_2942013
Rabbit monoclonal anti-Acetyllysine	PTM Bio, China	Cat# PTM-105RM; RRID: AB_3099509
Mouse monoclonal anti-Crotonyllysine	PTM Bio, China	Cat# PTM-502; RRID: AB_2877695
Rabbit monoclonal anti-Butyryllysine	PTM Bio, China	Cat# PTM-301; RRID: AB_2687946
Mouse monoclonal anti-Succinyllysine	PTM Bio, China	Cat# PTM-419; RRID: AB_2942099
Rabbit monoclonal anti-YTHDC1	Abcam, USA	Cat# ab259990
Rabbit monoclonal anti-IGF2BP1	Abcam, USA	Cat# ab290736
Rabbit monoclonal anti-PABPN1A	Abcam, USA	Cat# ab75855; RRID: AB_1310538
Mouse monoclonal anti-E2F2	Abcam, USA	Cat# ab70731; RRID: AB_2096783
Rabbit polyclonal anti-Ki67	Abcam, USA	Cat# ab15580; RRID: AB_443209
Rabbit polyclonal anti-LDHA	CST, USA	Cat# 2012; RRID: AB_2137173
Rabbit monoclonal anti-p300	CST, USA	Cat# 86377; RRID: AB_2800077
Rabbit monoclonal anti-HDAC3	CST, USA	Cat# 85057; RRID: AB_2800047
Mouse monoclonal anti-Bcl-2	CST, USA	Cat# 15071; RRID: AB_2744528
Rabbit monoclonal anti-Flag	CST, USA	Cat# 14793; RRID: AB_2572291
Rabbit monoclonal anti-HA	CST, USA	Cat# 3724; RRID: AB_1549585
Mouse monoclonal anti-HA	CST, USA	Cat# 2367; RRID: AB_10691311
Rabbit polyclonal anti-H3	CST, USA	Cat# 9715; RRID: AB_331563
Rabbit monoclonal anti-HIF1α	CST, USA	Cat#36169; RRID: AB_2799095
Rabbit monoclonal anti-HIF2α	CST, USA	Cat# 59973; RRID: AB_2799579
Rabbit polyclonal anti-β-Tubulin	CST, USA	Cat# 2146; RRID: AB_2210545
Rabbit polyclonal anti-β-actin	CST, USA	Cat# 4967; RRID: AB_330288
Rabbit monoclonal anti-Lamin B1	CST, USA	Cat#13435
Rabbit monoclonal anti-LDHB	Abmart, China	Cat# T58008
Anti-Rabbit Mouse IgG-HRP	Abmart, China	Cat# M21008
Anti-Mouse IgG for IP-HRP	Vazyme, China	Cat# RA1009-01
Anti-Rabbit IgG for IP-HRP	Vazyme, China	Cat# RA1008-01
Goat anti-Rabbit Alexa Fluor 488	Invitrogen	Cat# A32731; RRID: AB_2633280
Goat anti-Rabbit Alexa Fluor 594	Invitrogen	Cat# A32740; RRID: AB_2762824
Goat anti-Mouse Alexa Fluor 594	Invitrogen	Cat# A11032; RRID: AB_2762824
Donkey anti-Rabbit Alexa Fluor 647	Invitrogen	Cat# A32795; RRID: AB_2762835
Rabbit monoclonal anti-GAPDH-HRP	ABclonal, China	Cat# AC054
Rabbit monoclonal anti-Flag-HRP	ABclonal, China	Cat# AE095; RRID: AB_3095641
Anti-YTHDC1^{K82la} specific antibody	ABclonal, China	N/A
Bacterial and virus strains		
DH5α	Yeasen, China	Cat# 11803ES80
Biological samples		
Paired RCC and adjacent tissues	outdo Biotech Co., Shanghai	OD-CT-UrKid03-003
Paired ccRCC and adjacent tissues	outdo Biotech Co., Shanghai	HKid-CRC180Sur-01
Chemicals, peptides, and recombinant proteins		
DMEM medium	Gibco	cat#C11995500BT
RPMI-1640	Gibco	Cat# 10-014-CV
McCoy's 5A	Gibco	Cat# 10-050-CV

(*Continued on next page*)

Continued

REAGENT or RESOURCE	SOURCE	IDENTIFIER
Fetal bovine serum	Hyclone	Cat# SH30084.03
penicillin/streptomycin	Invitrogen	Cat# 15070063
NaLa	Sigma, USA	Cat# 1614308; Cas No. 867-56-1
Nicotinamide (NAM)	Sigma, USA	Cat# N9910
Puromycin	Sigma, USA	Cat# P8833
DAPI	Sigma, USA	Cat# D9542
Triton X-100	Invitrogen	Cat# HFH10
RIPA	epizyme	Cat# PC105
Cocktail	epizyme	Cat# GRF101
ECL	epizyme	Cat# SQ201
Anti-HA Magnetic agarose	Sigma, USA	Cat# SAE0197
Anti-Flag M2 beads	Sigma, USA	Cat# A2220
Flag-peptide	Sigma, USA	Cat# F3290
Crystal violet	Sigma, USA	Cat# C0775; Cas No. 548-62-9
3-BP	MCE, USA	Cat# HY-19992; CAS No. 1113-59-3
Sunitinib	MCE, USA	Cat# HY-10255[a]; CAS No. 557795-19-4
C646	MCE, USA	HY-13823; CAS No. H328968-36-1
HA-peptide	Beyotime, China	Cat# P9808
lactyl-CoA	ikekule, China	Cat# FM120; Cas No. 1926-57-4
Lipofectamine™ LTX	Invitrogen	Cat# 15338100
Actinomycin D	Invitrogen	Cat# 11805017
HighGene plus transfection reagent	ABclonal, China	Cat# RM09014P
Trichostatin A (TSA)	Selleck	Cat# S1045
Critical commercial assays		
RNA-Quick Purification Kit	Yishan Biotechnology, Shanghai	Cat# ES-RN001
Cell Counting Kit-8 (CCK-8)	Beyotime, China	Cat# C0037
RIP Kit	Bersinbio, China	Cat# Bes5101
m6A MeRIP Kit	Bersinbio, China	Cat# Bes5203
CLIP-qPCR Kit	Bersinbio, China	Cat# Bes3105
Annexin V-FITC Apoptosis Detection Kit	Beyotime, China	Cat# C1062S
Cell Cycle and Apoptosis Analysis Kit	Beyotime, China	Cat# C1052
Nuclear and Cytoplasmic Protein Extraction Kit	Beyotime, China	Cat# P0028
BeyoClick™ EdU Cell Proliferation Kit	Beyotime, China	Cat# C0078S
Hieff UNICON® qPCR SYBR Green Master Mix	Yeasen, China	Cat# 11200ES08
Lactic Acid (LA) Content Assay Kit	Solarbio, China	Cat# BC2235
MiniBEST Universal RNA Extraction Kit	Takara	Cat# 9767
PrimeScriptTM RT Master Mix	Takara	Cat# RR385A
PrimeSTAR® Max DNA Polymerase	Takara	Cat# R045Q
NE-PER Nuclear and Cytoplasmic Extraction Reagents	Thermo Fisher	Cat# 78833
Click-iT Nascent RNA Capture Kit	Thermo Fisher	Cat# C10365
RNASweAMI™ *In situ* Hybridization	Savorbio	Cat# GF003
FISH Kit	Bersinbio, China	Cat# Bes1001
Deposited data		
Proteome data	This paper	PXD053029
Lactylome data	This paper	PXD052772
PRM for YTHDC1 lactylation quantification	This paper	PXD058173
RNA-sequencing data	This paper	SRA data: PRJNA1120114
RIP-sequencing data	This paper	SRA data: PRJNA1120661

(*Continued on next page*)

Continued

REAGENT or RESOURCE	SOURCE	IDENTIFIER
WB and fluorescence raw data	Mendeley data	https://doi.org/10.17632/nxrv6sf8f8.1
Experimental models: Cell lines		
Human: ACHN	ATCC	CRL-1611™
Human: 769-P	ATCC	CRL-1933™
Human: 786-O	ATCC	CRL-1932™
Human: Caki-1	ATCC	HTB-46™
Human: Caki-2	ATCC	HTB-47™
Human: RPTEC	ATCC	PCS-400-010™
Human: OS-RC-2	Procell, China	CL-0177
Human: HEK293T	ATCC	CRL-11268
Experimental models: Organisms/strains		
Mouse: BALB/c nude	Vitalriver, China	N/A
Oligonucleotides		
Gene-specific primers for RT-PCR and RT-qPCR	This study	Table S3
siRNA and shRNA sequences	This study	Table S4
Recombinant DNA		
Plasmid: pcDNA3.1-YTHDC1-EGFP-Flag	This paper	N/A
Plasmid: pcDNA3.1-YTHDC1 K82R-EGFP-Flag	This paper	N/A
Plasmid: pcDNA3.1-YTHDC1 K82T-EGFP-Flag	This paper	N/A
Plasmid: pcDNA3.1-YTHDC1 K82Q-EGFP-Flag	This paper	N/A
Plasmid: YTHDC1 pLVX-shRNA-NEO	Youbio, China	N/A
Plasmid: pCDH-YTHDC1-3xFlag+PURO	This paper	N/A
Plasmid: pCDH-YTHDC1 K82R-3xFlag+PURO	This paper	N/A
Plasmid: pCDH-YTHDC1 K82T-3xFlag+PURO	This paper	N/A
Plasmid: pcDNA3.1-YTHDC1-3xFlag	This paper	N/A
Plasmid: pcDNA3.1-BCL2	This paper	N/A
Plasmid: pcDNA3.1-E2F2	This paper	N/A
Plasmid: pcDNA3.1-YTHDC1-HA	This paper	N/A
Plasmid: pcDNA3.1-P300-HA-HATs	Hongquan Zhang' lab	N/A
Plasmid: pcDNA3.1-CBP-HA-HATs	Hongquan Zhang' lab	N/A
Plasmid: pcDNA3.1-KAT5-HA-HATs	Hongquan Zhang' lab	N/A
Plasmid: pcDNA3.1-KAT2B-HA-HATs	Hongquan Zhang' lab	N/A
Plasmid: pcDNA3.1-KAT8-HA-HATs	Hongquan Zhang' lab	N/A
Plasmid: pcDNA3.1-Flag-HDAC1-9	Hongquan Zhang' lab	N/A
Software and algorithms		
GraphPad Prism 9	https://www.graphpad.com/	N/A
ImageJ	https://imagej.nih.gov/ij/	N/A
BioRender – Illustration tool	https://www.biorender.com/	N/A

EXPERIMENTAL MODEL AND STUDY PARTICIPANT DETAILS

Tissue collection

Tissue microarrays (TMAs) of RCC patients were purchased from Shanghai outdo Biotech Co., Ltd. All tissue samples were pathologically confirmed by certified pathologists. The complete data of patient characteristics are shown in Table S1. Written informed consent was obtained from all patients. The human materials used in this study were approved by the ethics committee of Shanghai outdo Biotech Co., Ltd. (protocol No. SHYJS-CP-1501001 and SHYJS-CP-1304010).

Female wild-type BALB/c xenograft-bearing nude mice aged among 4–6 weeks were housed in a specific-pathogen-free facility at Capital Medical University. All animal tissues were collected in accordance with the guidelines of the Institutional Animal Care and Use Committee of Capital Medical University (protocol No. AEEI-2023-299).

Cell culture and treatment

HEK293T, RPTEC, ACHN, 769-P, 786-O, Caki-1 and Caki-2 cells were purchased from the American Type Culture Collection (Manassas, USA). OS-RC-2 was obtained from Procell Biotech (Wuhan, China). HEK293T and RPTEC cells were maintained in DMEM medium. ACHN, 769-P, 786-O and OS-RC-2 cells were cultured in RPMI-1640 medium. Caki-1 and Caki-2 cells were maintained in McCoy's 5A medium. All media were purchased from Gibco Laboratories (Grand Island, USA) and were supplemented with 10% fetal bovine serum (HyClone, USA) and 1% penicillin/streptomycin (Invitrogen, Waltham, USA). Cells were cultured at 37°C and 5% CO_2. All the cell lines were tested for mycoplasma contamination, and no commonly misidentified cell lines were used. To induce hypoxia, cells were cultured in 1% oxygen condition or other oxygen conditions (20%, 10%, 5%, 2%) with incubator (Heracell™, ThermoFisher, USA). Cells were treated with NaLa (10/20 mM, Sigma, USA), 3-BP (10/20/30/40 nM, MCE, USA), and sunitinib (3 μM, MCE) for 24 h, TSA (1 μM, Selleck) and NAM (5 mM, Sigma, USA) for 4 h.

METHOD DETAILS

Immunofluorescence

Cells were seeded into confocal dish and washed with PBS for three times. Then cells were fixed with 4% methanol-free formaldehyde for 20 min and permeabilized with 0.3% Triton X-100 in PBS for 15 min at room temperature. After rinsing with washing buffer (0.1% Triton X-100 in PBS) for three times, the cells were blocked for 2 h with blocking buffer (5% BSA in washing buffer) and incubated with anti-YTHDC1^{K82la} (1:100), anti-HA (1:100), or anti-YTHDC1 (1:100) antibodies in blocking buffer overnight in 4°C. Next day, the cells were rinsed with washing buffer 3 times and incubated with the secondary antibodies conjugated with Alexa 488 or Alexa-594 (1:2000) at room temperature for 1 h. Then, the cells were washed with washing buffer for 3 times, incubated with DAPI (1:100) in PBS for 10 min and washed with PBS for 3 times. Images were visualized and analyzed with Leica TCS SP8 confocal microscope. Tissue immunofluorescence (IF) staining was performed with a similar scheme. Briefly, tissue sections were blocked and incubated overnight at 4°C with the respective primary antibody, followed by incubation with the corresponding fluorescent secondary antibody for staining. The antibodies used here include: Anti-L-Lactyllysine and Anti-YTHDC1^{K82la} specific antibody (1:100).

Western blotting

Western blotting (WB) was conducted as standard protocol.[31] RIPA (PC105, epizyme) buffer supplemented with a protease inhibitor cocktail (GRF101, epizyme) was used to lyse cells on ice for 20 min. Extracted proteins were heated to 100°C for 10 min and subjected to electrophoresis via 6–15% SDS-polyacrylamide gel electrophoresis (PAGE). Signals were detected using Western ECL Substrate (SQ201, epizyme). Antibodies information is shown in key resources table.

Transfection

Cells were seeded in culture dishes at approximately 50–60% confluency. On the following day, cells were transfected using transfection reagent according to the manufacturer's instructions. Transfected cells were harvested 24 hours after transfection for subsequent experiments. HEK293T cells were transfected with HighGene plus transfection reagent (ABclonal, Wuhan, China) and other cells were transfected with Lipofectamine LTX (Invitrogen) following the manufacturer's instructions.

Virus production and infection

As previously described, target lentiviral vectors were co-transfected with the packaging plasmids pSPAX2 and pMD2.G into HEK293T cells using HighGene Plus transfection reagent (ABclonal, Wuhan, China) according to the manufacturer's protocol. Viral supernatants were collected 48 hours post-transfection and filtered through 0.45 μm syringe filters (Millipore). Filtered viral particles were used to infect target cells. After infection, cells were selected with puromycin to establish stable cell lines.

EdU assay

Cells were cultured in confocal dishes for 24 hrs. The BeyoClick™ EdU Cell Proliferation Kit was used according to the manufacturer's protocol. Cells were incubated with 50 mM EdU solution in the cell culture incubator for 2 h. Following this, the cells were fixed in 4% paraformaldehyde, permeabilized with 0.3% Triton X-100, and then subjected to a Click reaction followed by Hoechst staining. After staining, observation and imaging were performed, and counts were obtained under a Leica SP8 confocal microscope.

Colony formation assay

Cells were seeded at a density of 500 cells per well in a 6-well plate. After 12 days of incubation, the colonies were fixed with 4% paraformaldehyde and stained with 0.05% crystal violet, subsequently were imaged with camera and statistically analyzed using GraphPad Prism 9.

Wound healing assay

Cells were seeded in 6-well dishes. When cells reached 100% confluency, serum-free medium were used to inhibit cell proliferation. A uniform scratch was made in the cell monolayer using a P-20 micropipette tip. The width of the wounded region was monitored and measured after 24 hrs to assess the rate of cell migration and wound closure. Image-J software to document cell migration.

Transwell assay

Cells in serum-free media were seeded into Transwell having a polycarbonate membrane coated with thin basement membrane (Corning® Matrigel® Basement Membrane Matrix, LDEV-free, for invasion). The lower chamber was filled with 10% FBS and RPMI medium. After a 24 h incubation, the Transwell system was stained with 0.05% crystal violet. The cells migrating to the lower chamber were imaged and statistically analyzed using GraphPad Prism 9.

CCK-8 assay

The cell proliferation was assessed using the Cell Counting Kit-8 (CCK-8) (Beyotime, China), as per the manufacturer's protocol. The cells were resuspended in 100 μL complete culture medium and plated into 96-well plates at a concentration of 2,000 cells per well. The plates were then incubated for a duration of 4 days. Subsequently, the medium was aspirated, and 110 μL of the CCK-8 solution (which consisted of 10 μL of CCK-8 reagent diluted in 100 μL of DMEM) was introduced and incubated for one hour at 37°C in the dark. The absorbance value was subsequently measured using an automated microplate spectrophotometer (Perkin Elmer, Enspire 2300) at a wavelength of 450 nm to determine the results and statistically analyzed using GraphPad Prism 9. CCK-8 was also utilized to assess cytotoxicity. Each well was resuspended with 10,000 cells in culture medium containing the drugs (3-BP or sunitinib), the absorbance value was measured after 24 hrs to calculate cell survival rate.

Xenograft

We performed three groups of xenograft tumor experiments. The first group included 10 BALB/c nude mice. Mice were either injected with NaLa (0.5 g/kg body weight) intraperitoneally or left untreated for seven days and all injected with ACHN cells. The number of days was recorded until the tumor reached 20 mm^3 in diameter. Post-tumor formation, administered NaLa/PBS intraperitoneally every five days. The second group included 12 BALB/c nude mice. A total of 1×10^6 ACHN cells stably transfected with $YTHDC1^{WT/KR}$ plasmid were injected subcutaneously on the back of BALB/c nude mice. The third group included 24 nude mice with the same conditions presented above and all injected with $YTHDC1^{WT}$-ACHN cells. When the tumor volume reached 60 mm^3, 3-BP (8 mg/kg body weight) and sunitinib (MCE, USA, 10 mg/kg body weight) were injected intraperitoneally every 2 days. Four weeks later, tumor weight and volume were measured and calculated after collection. All mice received an intraperitoneal injection of NaLa (0.5 g/kg body weight) every five days. Tumor volumes, measured along the major axis (a) and minor axis (b), were recorded weekly and calculated using the formula: $V = ab^2/2$. Mice were then sacrificed, and tumors were excised and weighed.

For *in vivo* metastasis studies, ACHN cells (5×10^5) stably transfected with empty vector or $YTHDC1^{WT/KR}$ plasmid were injected into the tail veins of 10 BALB/c nude mice. After 6 weeks, the mice were sacrificed and the lungs were harvested to assess metastasis.

LC-MS analysis

4D label-free quantitative LC-MS/MS analysis was performed by PTM BioLabs (Hangzhou, China).[2] To enrich modified peptides, tryptic peptides dissolved in NETN buffer were incubated with pre-washed antibody beads (Lot number 001, PTM Bio). The bound peptides were eluted from the beads with 0.1% trifluoroacetic acid. Finally, the eluted fractions were combined and vacuum-dried.

For LC-MS/MS analysis, the resulting peptides were desalted with C18 ZipTips (Millipore, USA) according to the manufacturer's instructions. The peptides were subjected to capillary source followed by the timsTOF Pro (Bruker Daltonics) mass spectrometry. Precursors and fragments were analyzed at the TOF detector, with a MS/MS scan range from 100 to 1700 m/z. The timsTOF Pro was operated in PASEF mode. The dynamic exclusion was set to 30 s. The resulting MS/MS data were processed using Maxquant search engine (v.1.6.15.0). Tandem mass spectra were searched against Homo_sapiens_9606_SP_20230103.fasta (20389 entries) concatenated with reverse decoy database. Trypsin/P was specified as cleavage enzyme allowing up to 2 missing cleavages. The mass tolerance for precursor ions was set as 20 ppm in first search and 200 ppm in main search. Carbamidomethyl on cysteine was specified as fixed modification, and methionine oxidation and protein N-terminal acetylation were specified as variable modifications. FDR was adjusted to < 1%.

Parallel reaction monitoring

To quantify the occupancy of YTHDC1 lactylation, quantitative Parallel Reaction Monitoring (PRM) was employed. ACHN cells transfected with YTHDC1-Flag were collected. YTHDC1 proteins were isolated using anti-Flag beads and then separated on a 10% SDS-PAGE gel, followed by Coomassie staining. The proteins were excised based on their molecular weight for mass spectrometric analysis. Tryptic peptides were loaded onto a custom-made reversed-phase analytical column (Reprosil-Pur 120 C18-AQ 1.9 μm; 17 cm length × 150 μm i.d.) connected to a Vanquish Neo - Orbitrap Fusion Lumos mass spectrometer. The mobile phase consisted of buffer A, which was 0.1% formic acid in water, and buffer B, which was 0.1% formic acid in 80% (v/v) acetonitrile. The flow rate was set at 600 nL/min over a gradient of 131 minutes. The following precursor ion lists were collected: PLSSSVSNNK(La)R Mass [m/z] 630.8308; PLSSSVSNNKR Mass [m/z] 594.8202; PLSSSVSNNK Mass [m/z] 516.7696. PRM data were manually curated within Skyline, with a cut-off value set at 0.99.

Immunoprecipitation

Cells were washed once with PBS and then lysed on ice for 30 min with Lysis Buffer for IP (Epizyme). The lysate was harvested by scraping the cells and centrifuged at 12,000 g for 20 min. The soluble fraction was collected, and the cell extract was mixed with anti-Flag M2 beads (Sigma, USA) or specified antibody plus Protein A/G-Agarose (Abmart) at a ratio of 1 mg of extract per 30 μL of agarose. After shaking overnight at 4°C, the beads were pelleted at 2,500 g for 3 min and washed three times with sample buffer. Finally, the samples were boiled in 1×SDS loading buffer (Epizyme) and WB was performed.

Cell cycle analysis

Flow cytometry was used to analyze cell cycle using propidium iodide (PI) staining (Cell Cycle and Apoptosis Analysis Kit, Beyotime). Cells were collected and washed once with PBS. Cells were fixed with cold 70% ethanol for 30 min at 4°C, followed by twice washes with PBS. The cells were resuspended in RNAse (100 μg/mL) and then stained with PI (50 μg/mL). The stained cells were analyzed using the BD LSRFortessa™ flow cytometer.

Fluorescence recovery after photobleaching

Living cells FRAP experiments were performed on Zeiss 880 with 488 nm laser. Briefly, photobleaching was performed in the central region of interest (ROI) of cells using the laser line. Fluorescence recovery was monitored every 1 s for 50 s immediately after photobleaching. The fluorescence intensity and the images were recorded by the FRAP module in the ZEISS ZEN 3.9 software. The prebleached fluorescence intensity was normalized to 1. Data analysis and visualization were performed using ImageJ software.

Protein purification

The plasmids containing the full-length human YTHDC1 sequence with a Flag tag at the C-terminus (CT) and p300 sequence with HA tag at the CT were transfected into HEK293T cells for protein expression. After 48 hrs, the cells were harvested. The proteins were purified using Anti-Flag/HA Affinity Gel (Beyotime, China) and eluted with 3×Flag Peptide (Sigma, USA) or HA Peptide (Beyotime, China) according to the manufacturer's instructions. The expression of the target protein was analyzed using SDS-PAGE, and the protein was flash-frozen in liquid nitrogen and stored at -80°C. The expression and purification results of the YTHDC1 mutant were similar to the wild-type protein.

In vitro lactylation assay

The YTHDC1 fusion proteins were incubated with p300 proteins in reaction buffer (50 μM Tris-HCl, 1 mM DTT, 10% glycerin) with 20 mM lactyl-CoA (ikekule, China). Reactions were incubated at 37°C for 30 min. Samples were denatured by heating at 100 °C for 10 min and immunoblotted with indicated antibodies.

RNA-seq and RIP-seq

RNA was extracted from three replicates of cells stably overexpressing YTHDC1-WT and YTHDC1-KT using TRIzol reagent (Invitrogen, 15596026). mRNA was enriched from the extracted RNA using magnetic beads with Oligo(dT). The RNA was fragmented using a fragmentation buffer, followed by reverse transcription with random N6 primers to generate single-stranded cDNA. This was then converted into double-stranded cDNA by synthesis of the second strand. The ends of the double-stranded cDNA were blunt-ended and 5' phosphorylated, and the 3' ends were formed with sticky ends overhanging a single "A" base. These were ligated to adaptors with protruding "T" overhangs at the 3' end. The ligated products were amplified by PCR using specific primers. The PCR products were denatured into single strands and circularized into single-stranded circular DNA libraries using a bridge PCR primer. The constructed library was quality-assessed and sequenced using Illumina Novaseq 6000. The raw sequencing data were subjected to quality control (QC) and analyzed. HISAT was used as the reference genome. RNA-seq was performed in BGI Genomics Co Ltd (Shenzhen, China).

For RIP-seq, the lysate from YTHDC1-Flag-ACHN cells was incubated with anti-Flag antibody. IgG was used as an internal control. RNA sequencing library was constructed using the NEBNext Ultra II Direct RNA Library preparation Kit. The library was sequenced on Illumina NovaSeq 6000 platform with 150 bp paired-end reads. RIP-seq was performed in Seqhealth (Wuhan, China).

RT-PCR

For reverse transcription-polymerase chain reaction (RT-PCR), total RNA was extracted from cultured cells using MiniBEST Universal RNA Extraction Kit (TaKaRa, Japan). The extracted RNA was then reverse transcribed into cDNA using the HiScript II 1st Strand cDNA Synthesis Kit (Vazyme, China). The primer sequences were listed in Table S3.

RT-qPCR

The PrimeScript™ RT reagent Kit with gDNA Eraser from TaKaRa (RR047A) were used for cDNA synthesis. Quantitative real-time PCR (RT-qPCR) was performed using SYBR Green (TaKaRa). The internal reference gene used was GAPDH. The primer sequences for RT-qPCR were listed in Table S3.

RIP and MeRIP assays

ACHN or YTHDC1$^{WT/KR/KT}$ ACHN cells were collected (2×10^7 cells were used per IP reaction), and were washed twice with pre-cooled PBS. The cells were lysed in lysis buffer and placed on ice for 30 min. Following this, DNAase was added, and the supernatant was collected after high-speed centrifugation. Anti-IgG, anti-Flag or anti-m6A antibodies were incubated with magnetic beads at room temperature for 30 min according to the instructions of the RNA/Methylated RNA immunoprecipitation Kit (BersinBio, China). Then, the antibody-bead complexes were incubated with cell lysates at 4°C overnight. The bound RNAs were eluted and reverse transcribed to cDNA and subsequently detected by RT-PCR or RT-qPCR.

Cross-linking immunoprecipitation q-PCR

CLIP-qPCR was performed using the CLIP-qPCR Kit (BersinBio, China) according to the manufacturer's protocol. Briefly, YTHDC1-FLAG ACHN cells (2×10^7 per IP) were incubated with 4-thiouridine (4sU) prior to crosslinking. Cells were then irradiated with 365 nm UV light at an energy dose of 0.15 J/cm^2 for 10 minutes to induce RNA–protein crosslinking. After UV treatment, immunoprecipitation was performed in our CLIP protocol. RNA was extracted from the immunoprecipitated complexes, and a poly(A) tail was added to the 3′ end of the RNA. The tailed RNA was then reverse transcribed into cDNA. RT-qPCR was performed using forward primers targeting the 5′ UTR, CDS and 3′ UTR regions of *BCL2* and *E2F2* mRNAs, along with a universal reverse primer provided in the kit. The primer sequences for RT-qPCR were listed in Table S3.

Nascent RNA assay

YTHDC1$^{WT/KR/KT}$ ACHN cells were incubated with EU for 1 h and then harvested. Total RNA was purified using Trizol. RNA was biotinylated using the Click-iT labeling buffer at 4°C, the nascent RNA was enriched using streptavidin magnetic beads. The Click-iT Nascent RNA Capture Kit from Invitrogen was used and the Nascent RNA was determined by RT-qPCR in accordance with the manufacturer's protocol.[25]

mRNA stability assay

YTHDC1$^{WT/KR/KT}$ ACHN Cells were treated with 5 μg/mL actinomycin D (Sigma, USA) to block transcription for 0, 1, 2, 4 and 6 h. RNA was extracted from the cells, and *E2F2* or *BCL2* mRNA was assessed through RT-qPCR.

Cellular fractionation and RNA isolation

Cells underwent fractionation employing NE-PER Nuclear and Cytoplasmic Extraction Reagents (ThermoFisher, USA). Subsequent to the separation of cytoplasmic and nuclear components, thorough washing with PBS was performed. RNA extraction was carried out using the RNA-Quick Purification Kit (Yishan Biotechnology, Shanghai) and subjected to DNase I treatment before elution in water.

RNA-Fluorescence *in situ* hybridization in conjugation with fluorescent immunostaining

The specified cells were fixed in confocal dishes using 4% paraformaldehyde. Following the manufacturer's instructions (RNASweAMI™ *In situ* Hybridization Protocol, Savorbio), RNA *in situ* hybridization was first performed using RNASweAMI. The RNASweAMI probe targeting human *BCL2* was designed and produced by Savorbio. After the *in stiu* hybridization was completed, the dishes were rinsed twice and subjected to immunostaining. During the immunostaining, protease K was used for a brief permeabilization. Subsequently, staining for anti-YTHDC1 or anti-PABPN1 was performed according to the IF protocol, followed by DAPI counterstaining. The image was performed using a Leica SP8 Confocal Microscope system, analyzed in the LAS X software.

FISH was conducted to visualize the localization of *BCL2* mRNA. A custom-made Cy3-labeled *BCL2* probe was designed and synthesized by Servicebio Biotechnology (Wuhan, China). The FISH Kit from BersinBio was utilized to detect the signals emitted by the Cy3-labeled probe, following the manufacturer's protocols. The imaging of the FISH signals was performed using a Leica SP8 Confocal Microscope system, analyzed in the LAS X software.

Apoptosis analysis

After treatment with the drug, 10^5 cells were collected and then 5 μL of Annexin V-FITC and 10 μL of PI staining solution were added (Annexin V-FITC apoptosis detection kit, Beyotime). The mixture was incubated in the dark at room temperature (20–25°C) for 20 min, after which it was placed on ice. The stained cells were analyzed using the BD LSRFortessa™ flow cytometer.

QUANTIFICATION AND STATISTICAL ANALYSIS

All data are presented as mean ± standard deviation (SD), and analyzed using GraphPad Prism 9 software for two-tailed *t*-tests, one-way analysis of variance (ANOVA) or two-way ANOVA. Statistical significance was considered at $p < 0.05$ (*), $p < 0.01$ (**), and $p < 0.001$ (***).